universität wien

MASTERARBEIT | MASTER'S THESIS

Titel | Title

Developing an in-situ Laser System for an Aberration-Corrected Scanning Transmission Electron Microscope

verfasst von | submitted by

Fabian Kraft BSc

angestrebter akademischer Grad | in partial fulfilment of the requirements for the degree of

Master of Science (MSc)

Wien | Vienna, 2025

Studienkennzahl lt. Studienblatt | Degree programme code as it appears on the student record sheet:	UA 066 876
Studienrichtung lt. Studienblatt | Degree programme as it appears on the student record sheet:	Masterstudium Physics
Betreut von | Supervisor:	Assoz. Prof. Dr. Toma Susi

Zusammenfassung

In dieser Arbeit entwickeln wir ein *in-situ* Lasersystem für ein aberrationskorrigiertes Rasterdurchstrahlungselektronenmikroskop inklusive eines Designs des optischen Systems und einer Software-Hardware-Schnittstelle zur Steuerung des Lasers. Dieses Lasersystem erzeugt einen elliptischen Punkt mit einem Durchmesser ca. $30\,\mu m$ auf der Probe im Probenhalter. Wir messen diesen Laserspot mittels Laserbestrahlungseffekten auf einem Quantifoil Probenträger aus amorphen Kohlenstoff. Das Hauptdesignziel dieses Lasersystems ist es, Proben für elektronenmikroskopische Bildgebung zu reinigen. Wir überprüfen die Reinigungsfähigkeiten, die uns dieses System bietet, mit einlagigem Graphen auf einem Quantifoil Probenträger von Graphenea. Das Lasersystem ist auch dazu in der Lage, andere *in-situ* Experimente durchzuführen, eines davon ist stimulierte Elektronenenergie-Gewinn-Spektroskopie (sEEGS). Nachdem wir verschiedene Experimente evaluiert haben, können wir sagen, dass diese Art von Experimenten in unserem derzeitigen Lasersystem nicht möglich sind. Jedoch können wir Graphenproben mit einem relativen Reinigungseffekt bis zu $30\,\%$ reinigen.

Abstract

In this thesis, we develop an *in-situ* laser system for an aberration-corrected scanning transmission electron microscopy including design of the optical system and the software-hardware interface to control the laser. This laser system has an elliptical spot size of about $30\,\mu m$ in diameter on the sample sitting in the microscope sample stage. We measure this using laser irradiation effects on a Quantifoil support grid made from amorphous carbon. The main design goal of the laser system is to atomically clean samples for electron microscopy imaging. We evaluate the cleaning capability of the system with single-layer graphene on Quantifoil sourced from Graphenea. The laser system can also perform other *in-situ* experiments, one of which is stimulated electron energy gain spectroscopy (sEEGS). After evaluating various experiments, we conclude that this kind of study is not feasible within the current laser system. However, we manage to clean graphene samples, with a cleaning effect up to $30\,\%$.

Acknowledgments

I want to thank my supervisor, Toma Susi, for his input and corrections in scientific writing. He also provided insight into the scientific community and enabled me to travel to conferences. I especially want to thank him for his confidence and patience during the development of the laser system. Secondly, I want to thank Kimmo Mustonen and Manuel Längle for their support with the Nion UltraSTEM 100 and the debugging of the system, which they did with great patience. I especially thank Manuel Längle for his help in the experiment design and the discussions about this project, without this, I would not have been able to finish this work. Also, I sent a huge thanks to Clemens Mangler for his help and support in using the Nion UltraSTEM 100. A special thanks also goes to Tristan Nagy and Morris Weimerskirch from the Department of Physical Chemistry for providing me space in their optics lab and helping and advising me with any questions regarding the optical design. I thank Gerald Prager and Michael Czirkovits from the faculty's workshop for crafting the laser system's mechanics and helping me with the design of the mechanics and electronics.

Finally, I want to thank everyone around me for supporting me in my studies, especially my parents. Thank you all for supporting me during my best and worst, the "Sudicenter crew", and my friends for the regular meetings in Clash.

Only one laser controller and two Raspberry Pis were destroyed during this work.

Contents

Acronyms

ADC	analog-digital converter
ADF	annular dark-field
AFM	atom-force microscope
AOM	accustic-optical modulator
API	application programing interface
CAD	computer-aided design
CANVAS	controlled alteration of nanomaterials in vacuum down to the atomic scale
CCD	charge-coupled device
CL	cathod luminesence
CNC	computerized numerical control
CNT	carbon nanotubes
CVD	chemical vapour deposition
DPSS	diode-pumped solid-state
DSLR	digital single-lens reflex
DTFT	discrete-time Fourier transformation
DWCNT	double-wall carbon nanotube
EDX	energy-dispersive x-ray spectrosopy
EEGS	electron energy gain spectroscopy
EELS	electron energy loss spectroscopy
EOM	electric-optical modulator
FFT	fast Fourier transformation
FPGA	field programmable gate array
FWHM	full-width half-maximum
GPIO	general purpose input output
GUI	graphical user interface
HAADF	high-angle annular dark-field
hBN	hexagonal boron nitride
iCCD	intensified charge-coupled device
IPA	isopropyl alcohol
laser	light amplification by stimulated emission of radiation
LED	light emitting diode

MAADF	medium-angle annular dark-field
MQ	messageing queue
NMG	nanomaterials group
OEM	original equipment manufacturer
PMMA	poly methyl methacrylate
PoC	proof of concept
PWM	pulse-width modulation
RGB	red-green-blue
SE	secondary electrons
sEEGS	stimulated electron energy gain spectroscopy
sEELS	stimulated electron energy loss spectroscopy
SEM	scanning electron microscope
SLR	single-lens reflex
STEM	scanning transmission electron microscopy
SWCNT	single-wall carbon nanotube
TEM	transmission electron microscope
TEMM	transverse electromagnetic mode
TTL	transistor-transistor logic
UHV	Ultra High Vacuum
Vcc	voltage at the common collector
ZLP	zero-loss peak

List of Figures

List of Tables

1 Introduction

Recent developments in aberration-corrected electron microscopy have led to resolution improvements, which made it possible to study two-dimensional materials and their physical properties on an atomic level. We achieve this in scanning transmission electron microscopy (STEM) by reducing the probe size to 1 Å, therefore enabling single-atom detection and spectroscopy. The Nion UltraSTEM 100 has multiple possibilities for *in-situ* experiments, including multiple sample entry ports, viewports, and electrical pass-throughs to the sample enabling us to design and carry out various *in-situ* experiments. We can use electrical sample holders to measure the resistance of the sample. The viewports enable us to couple in optics, and we can use the side entry port for a vacuum transfer system [1].

In this thesis, we develop an *in-situ* laser system for an aberration-corrected scanning transmission electron microscopy (STEM), which will be part of the controlled alteration of nanomaterials in vacuum down to the atomic scale (CANVAS) system. We use those possibilities to design our laser setup mounted on Al-profiles at the place shown in Figure 1.1 (b). The electrical sample holder helps with the alignment, the laser couples in through the viewport (Figure 1.1 (a)), and the side-entry enables the sample exchange within the vacuum system. The laser system and its components are further discussed and documented. The goal of this thesis is a laser system with a laser spot size on the sample of a maximal diameter of 40 µm and its illumination time is controllable within the precision of 100 µs. The Nion user PC controls the system from outside the microscopy room via ethernet, and users use the implementation into the Nion Swift graphical user interface (GUI).

1.1 *In-situ* laser experiments

Howie already discussed the combination of lasers and electron microscopes in 1999 [2], as electron microscopes achieve a high spatial resolution but suffer from poor energy resolution, and light spectroscopy and microscopy have high energy resolution but poor spatial resolution. The combination of both methods enables a high resolution in both domains. There have been multiple attempts to implement these technologies.

We evaluate the laser system for its feasibility to carry out stimulated electron energy gain spectroscopy (sEEGS) experiments and exploit photon-electron coupling. We further discuss other possible use cases for *in-situ* experiments.

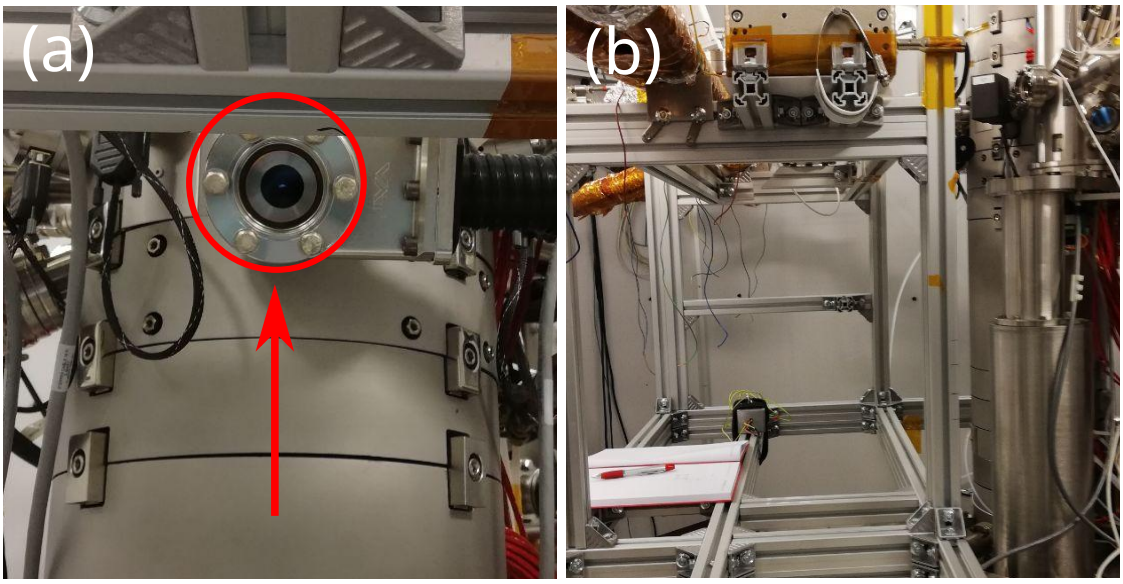

Figure 1.1: (a) Front view of the Nion UltraSTEM 100, where the red circle marks the viewport used to couple in the laser. (b) Side view of the mechanical support for the laser system (the STEM is on the right).

1.2 Cleaning of 2D materials

With atomic resolution, we are highly sensitive to any contamination, leading to the need for clean samples. One way to achieve this cleanness is by baking them before entry into the microscope. However, any *ex-situ* heat treatments can cause damage to the sample. Tripathi already established *pre-situ* laser cleaning, keeping the sample in a vacuum, minimizing the recontamination with airborne hydrocarbons, and the ambient expose may cause recontamination. However, this method needs constant sample transfer between the cleaning chamber and the STEM to verify the cleaning process. Also, mobile contamination can migrate to the previously cleaned areas while imaging, thus needing cleaning again [3].

An *in-situ* laser system will enable us to clean samples inside the STEM. We, therefore, do not need to transfer the sample again and obtain instant verification of the cleaning results, keeping recontamination to a minimum. A well-aligned laser also cleans the exact area we are imaging and interested in without affecting the surrounding areas on the sample.

In this thesis, we evaluate the capability of the *in-situ* laser system for cleaning single-layer graphene and find the optimal parameters for cleaning. The cleaning process also has aloof effects, which we study by creating a cleaning effect map.

2 Background

In this chapter, we introduce the theoretical background of this thesis. First, we introduce the sampling theorem. We further describe the used materials and their properties and the theoretical foundation of the methods such as electron microscopy and lasers. As this thesis also studies the feasibility of photon-electron coupling within the system, we discuss previous studies on this topic and introduce the theory of stimulated electron energy gain spectroscopy (sEEGS). We also give an overview of methods for sample cleaning and discuss their advantages and disadvantages.

2.1 Data acquisition and sampling

All modern detectors are pixelated or sample a discrete time series. We use the sampling theorem based on the discrete-time Fourier transformation (DTFT) to estimate the resolution at a given sample rate. A DTFT describes discrete sampling as a Fourier transformation of a continuous signal. This theorem is band-limited by an upper bound.

The DTFT is a discrete non-periodic Fourier transformation with an upper band limit because the number of discrete channels (N) is finite. X_k are the Fourier transformed values corresponding to the x_n in real space:

$$X_k = \sum_{n=0}^{N-1} x_n e^{\frac{-i2\pi}{N}kn} \ , \tag{2.1}$$

where n is the channel transforming and k is the index of the resulting Fourier space.

From the inverse DTFT

$$x_n = \frac{1}{N} \sum_{n=0}^{N-1} X_k e^{(\frac{i2\pi kn}{N})} \tag{2.2}$$

we deduct that a band-limited signal with the highest frequency ω_{max} is completely reconstructable if the sample rate T satisfies

$$\omega_{\text{max}} = \frac{1}{2T} \ . \tag{2.3}$$

If $\omega_{\text{max}} = \omega_{\text{Nyquist}}$ we call this the Nyquist-frequency [4].

An analog-digital converter (ADC) is an example of a device sampling using this theorem. Also, pixelated detectors represent a type of sampling. In a line detector like traditional spectrometers, the pixel numbers represent N in the DTFT.

Multidimensional detectors fulfill the Petersen-Middleton theorem, the multidimensional expansion of the Nyquist-Shannon Sampling theorem.

A function $f(\cdot)$ can be exactly reconstructed when sampled with a lattice $\Lambda \in \mathbb{R}^n$ if

$$\Omega \cap \{x + y : y \in \Omega\} = \emptyset \quad \forall\, x \in \Gamma \setminus \{0\} \tag{2.4}$$

where Γ is the reciprocal lattice of Λ and Ω is the set that limits the wave number of $f(\cdot)$. Ω is therefore a Fourier transform of $f(\cdot)$ with its highest frequency ω_{max}. [5]

Any sampled feature using a sampling rate defined by the lattice Λ can be reconstructed from its multidimensional DTFT if the set Ω and any of its sets shifted by any element of Γ do not overlap. This results in the highest frequency in Γ being bigger than $2 \cdot \omega_{max}$.

2.1.1 Detector

We can describe line detectors and time series using one-dimensional sampling and, therefore, can calculate the optimal sampling rate to measure our desired feature size.

Multidimensional sampling can describe pixelated detectors, such as cameras or direct electron detectors. Integral detectors, in combination with a scanning method, are either time-series or, in the case of STEM, pixelated detectors where each scan performed is interpreted as one pixel. We also can use multidimensional sampling for a combination of scanning and pixelated detectors, as we have, for example, in spectroscopy. We describe this as 3D sampling.

2.2 Material

2.2.1 Graphene

Although graphite is a widely available material, mostly known for its use in pencils, we did not know the exact structure until 30 years ago. Some theoretical thoughts about single graphite sheets have been made in the 1940s [6]. But it was widely believed that a 2D-material is not thermodynamically stable by itself [7, 8] and therefore only can exist as a surface on a substrate like SiO. However, in 2004, free-standing graphene was isolated as a monolayer by Novoselov and Geim [9]. Its stability is due to its corrugation into the third dimension as shown by Meyer in 2007 [10, 11]

Carbon (C) has of six electrons and in its ground state, it has an orbital configuration of $1s^2 2s^2 1p_x^1 1p_y^1$. The s-orbitals are spherical and the p-orbitals are orthonormal to each other. Therefore, carbon can hybridize into three configurations. The sp^3 configuration enables four σ bonds such as we find in CH_4, the sp^2 leads to three σ bonds and one π bond as found in vinyl ($CH_2{=}CH_2$) and finally the sp^1 configuration enables one σ bond and three π bonds as in acetylene ($CH{\equiv}CH$). In a carbon-only material, the sp^3 crystal has a diamond structure, the sp^2 graphite with the π bonds responsible for electrical conductivity and in Van der Waals bonding

of the sheets and the sp^1 hybridization into carbyne with the π bonds acting as free electron-gas [12].

As a result of the sp^2 configuration, the carbon atoms have three covalent bonds at an angle of $120°$ leading to a honeycomb-like lattice. The π bond from the p_z orbital delocalizes on the surface. The σ bonds lead to the outstanding mechanical properties of graphene.

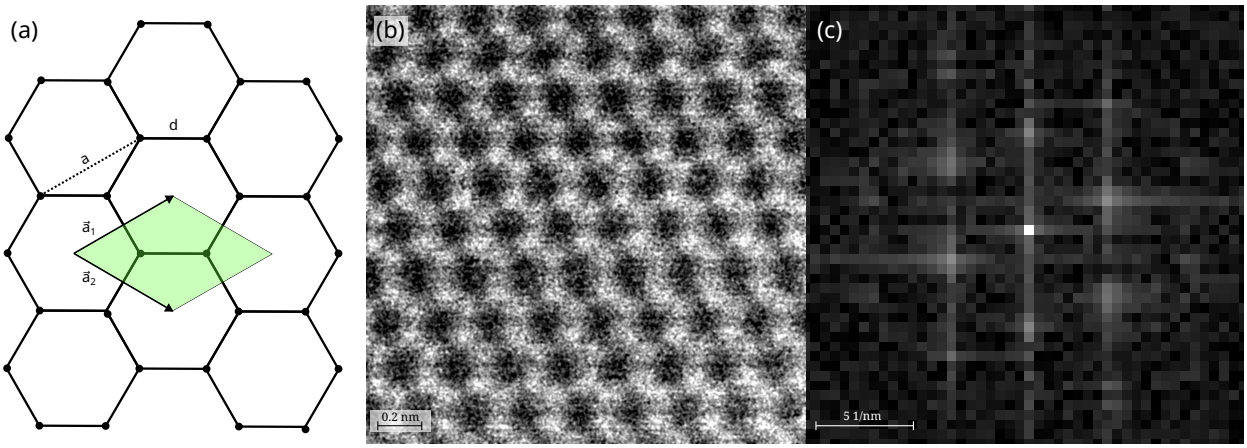

Figure 2.1: Structure of graphene: (a) Honeycomb lattice with its base vectors $\vec{a_1}$ and $\vec{a_2}$. The unit cell is marked green, a is the lattice constant, and d is the minimal atom distance. (b) Medium-angle annular dark-field (ADF) image of graphene and (c) its Fourier transformation revealing the hexagonal structure.

As shown in Figure 2.1, the lattice constant a of graphene's honeycomb lattice is 2.46 Å and the distance between two neighboring atoms is $d = 1.42$ Å. The base vectors $\vec{a_1}$ and $\vec{a_1}$ of graphene are therefore:

$$\vec{a_1} = \sqrt{3}d \begin{pmatrix} \frac{\sqrt{3}}{2} \\ \frac{1}{2} \end{pmatrix} \ , \ \vec{a_2} = \sqrt{3}d \begin{pmatrix} \frac{\sqrt{3}}{2} \\ -\frac{1}{2} \end{pmatrix} \ . \tag{2.5}$$

The green area shows the unit cell containing two atoms. We see the reciprocal lattice using a fast Fourier transformation (FFT) analysis as shown in Figure 2.1 (c). The reciprocal vectors $\vec{b_1}$ and $\vec{b_2}$ of graphene are further defined as:

$$\vec{b_1} = \frac{2\pi}{3d} \begin{pmatrix} 1 \\ \sqrt{3} \end{pmatrix} \ , \ \vec{b_2} = \frac{2\pi}{3d} \begin{pmatrix} 1 \\ -\sqrt{3} \end{pmatrix} \ . \tag{2.6}$$

Graphene has a superior thermal conductivity (5×10^3 $\mathrm{W\,m^{-1}\,K^{-1}}$) in-plane [13] and also unique electrical properties. One of its famous electrical properties is the 0 eV band gap [9], which makes it the perfect material for optical studies. Graphene is extremely mechanically and thermally stable, which makes it the perfect material for fundamental studies and single-atom observations.

There are two widely used methods to produce graphene. One is the original top-down method of exfoliating graphene from graphite. The other one is a bottom-up method using chemical vapour deposition (CVD).

To obtain a high quantity of high-quality graphene CVD is used. There are many recipes, but as an example, methane (CH_4) is put into a so-called CVD-reactor and flows over a catalytic surface and reacts to form graphene and H_2. Metals like Ni, Pt, and Cu are widely used as catalytic materials, especially Cu in [111] orientation is favored in large single-layer graphene production. We can control this process by tweaking the CH_4 flow rate, the reactor temperature, and the CH_4 concentration. CVD produces large graphene flakes in large quantities and are therefore commercially available and relatively cheap [14]. We source the samples with CVD used in this thesis from Graphenea.

Due to the weak v an der Waals bonding between the layers, materials such as graphene can be separated sheet by sheet, for example, while writing with a pencil. For pristine graphene, one can use adhesive force to separate the graphene layers from each other until only one layer is left. To create those adhesive forces, we can use scotch tape, as it was already done at the discovery of graphene [9]. The "scotch tape" method produces small "flakes" of one or more layer thicknesses with a size of a few μm^2. After transfer to supporting materials like SiO_2 and then onto transmission electron microscope (TEM) grids using isopropanol, one analyses graphene in a scanning transmission electron microscopy (STEM) [15]. These "flakes" are significantly smaller than the laser spot.

2.2.2 Carbon nanotubes

We can picture graphene like a piece of paper because it is a 2D material. We also can imagine rolling the sheet into a tube. These tubes of rolled-up graphene are called carbon nanotubes (CNT) and also have sp^2 hybridization [16]. Therefore, electrons, plasmons, and phonons are higly anistropic and are mainly active along the tube axis. Defects such as dopants, joints, or end-caps affect the band structure of these tubes and can tune the tubes.

Carbon nanotubes CNT can be described as rolled-up graphene sheets. As shown in Figure 2.2 (a), we describe the lattice orientation with a chiral vector C_h for a CNT

$$C_h = ma_1 + na_2 \ , \tag{2.7}$$

where ma_1 and na_2 are integer multiple of graphene's base vectors a_1 and a_2. Therefore, we can define a chiral angle θ as:

$$\theta = \tan^{-1}\left(\frac{\sqrt{3}m}{m+2n}\right) \ . \tag{2.8}$$

If the chiral angle θ is $0\,^\circ$, the configuration is called "armchair". If the chiral angle is 30°, "zigzag".

Due to their structure, CNTs have quasi one-dimensional properties. CNTs also possess a high tensile strength, making them useful as a support grid. Depending on their configuration, single-wall carbon nanotube (SWCNT) have metallic or semiconductive electrical properties. We consider CNT a semiconductor if

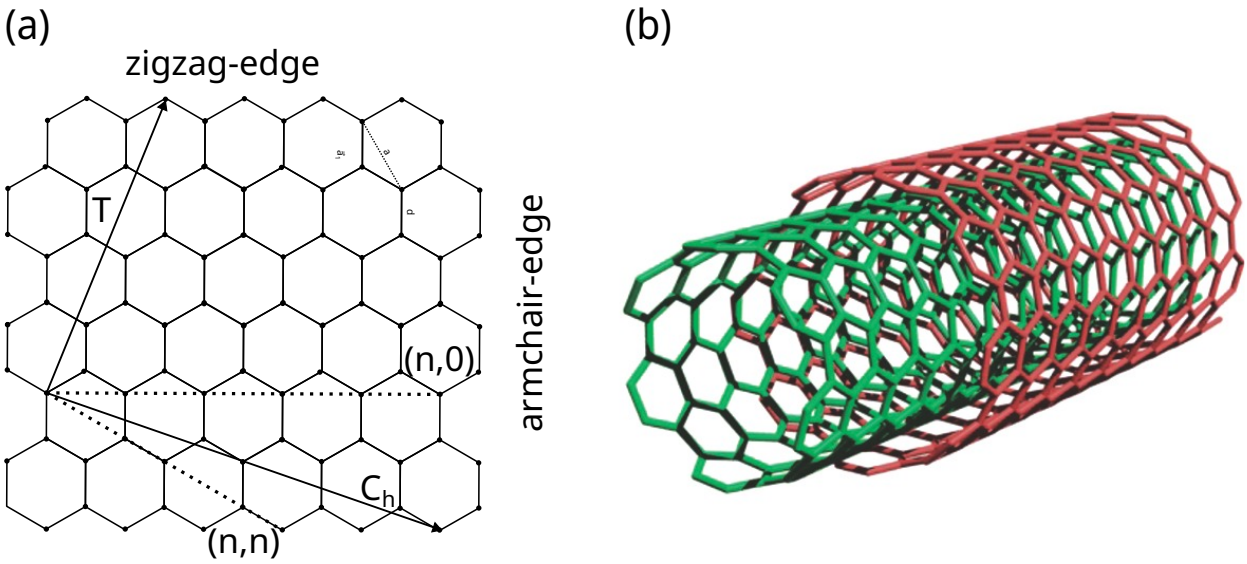

Figure 2.2: Carbon nanotube (CNT):(a) Carbon nanotube rolled from a graphene sheet. T is the translational and C_h the chiral vector of the CNT. (b) Example of a double-walled CNT taken from [17].

$$(n-m) \mod 3 = 0 \ , \tag{2.9}$$

where n and m are integer multiples of graphene's base vectors. We consider them to be metallic otherwise. The heat conductivity of a carbon nanotube film is $5\,\mathrm{W\,m^{-1}\,K^{-1}}$ and therefore significantly poorer than the heat conductivity of graphene [18].

If a CNT is inside another CNT along the same axis, we call this a double-wall carbon nanotube (DWCNT). We describe their structure with their chiral vectors using the notation (inner)@(outer) tube: $(n,m)@(n_0,m_0)$. In DWCNTs, both of the CNTs can be either metallic or semiconductor, with configurations $M@M$, $M@S$, $S@S$, and $S@M$. Depending on their inter-tube distance, the π bonds can interact and influence the properties of both CNTs [17] (Figure 2.2 (b)). The inner tube in a DWCNT is often defect-free [19] because the outer tube acts as a chemical shield for this inner tube. The inner tube structure defines the inner plasmonic states of the DWCNT, while the outer CNT defines the outer plasmonic behavior. We can produce DWCNT by CVD to grow a CNT inside of another outer tube. DWCNTs are more robust than SWCNTs. Also, semiconductive DWCNTs have lower bandgaps than their SWCNTs counterparts. Optical excitation can occur at 480–750 nm (1.45–2.55 eV) depending on the plasmonic structure of the DWCNT [17].

Because of their 1D structure, CNTs behave like dipole antennas for high-frequency electromagnetic fields such as light [20, 21]. For oriented MWCNT, this antenna effect is polarization-dependent. Because a laser is polarized, it can affect certain CNTs in a CNT-network perpendicular to the laser's polarization[20–22]. A carbon nanotube absorbs the energy of this light and transfers it into heat, possibly leading to its thermal destruction [23, 24].

Carbon nanotube networks consist of multiple carbon nanotubes which are connected to each other. These nanotubes are randomly oriented and connected by van der Waals bonds.

2.2.3 Amorphous carbon

Amorphous carbon is a highly disordered material. Therefore, carbon exists in various combinations, and all sp1, sp2, and sp3 hybridization occurs. In this amorphous phase, graphene nano-crystals, diamonds, and benzene can exist. Also, amorphous materials do have a high density of defects [25, 26].

We use thin amorphous carbon films as support grids for graphene and stand-alone samples. The heat conductivity of these films is orders of magnitude smaller than graphene's. The films used have a thickness up to 20 nm and a heat conductivity up to 1.43 $\mathrm{Wm^{-1}K^{-1}}$ [27].

2.3 Electron-matter interaction

2.3.1 Electron scattering

When an electron interacts with a material, it can be scattered. We divide scattering processes into inelastic and elastic. In elastic scattering, the energy of the electron stays almost unchanged. Electrons can be scattered at an angle or deflected back to their source, then called backscattered. Inelastically scattered electrons change their energy by gaining energy from or transferring energy to the material. We can detect both using electron spectroscopies such as electron energy loss spectroscopy (EELS) and electron energy gain spectroscopy (EEGS). The energy lost can also be measured by energy-dispersive x-ray spectrosopy (EDX) and cathod luminesence (CL).

Elastic scattering occurs when the probe electron hardly loses energy, but this scattering changes the path of the probe electron. We distinguish electrons scattered at an angle and completely backscattered electrons. An annular dark-field (ADF) detects scattered electrons at a specific angle. A backscatter detector detects electrons scattered to nearly 180° angle back towards the probe source.

When inelastic scattering occurs, the electron changes its energy during the process. The probe achieves this by bringing electrons to higher levels, ejecting secondary electrons (SE), or interacting with either plasmons or phonons. Plasmons are quantum quasiparticles representing collective electronic oscillation modes in a material. Their free path is typically ≈ 100 nm, and they have an energy of typically $5 - 25$ eV.

Phonons are also virtual quantum objects representing thermodynamical vibrational modes. Their energy typically is in the range of 100 meV. We can study them using high-resolution EELS or optical spectroscopy [28].

Secondary electrons SE are ejected from their orbit by inelastic scattering. This leaves a hole

whose filling with another electron typically emits radiation. The SE themselves and the emitted radiation can be detected.

2.3.2 Knock-on damage

An electron beam in an electron microscope can damage the sample. The beam can excite residual vacuum molecules to chemically etch the sample or it can knock out single atoms. This knock-on damage requires a significant beam energy. For CNTs, the reported beam energy for knock-on damage is in the range of $90 - 100$ keV [29, 30].

2.4 Electron microscopy

2.4.1 Why electron microscopy?

The Abbe limit defines the resolution of a microscope as follows:

$$d = \frac{\lambda}{2n\sin(\alpha)} \ , \tag{2.10}$$

where d is the minimal feature size that can be resolved, n is the refractive index, and α is the angle between the aperture and feature. For visible light, this limits the resolution to a few hundred nm.

Electron microscopes use an electron beam as a probe instead of light. Due to the Abbe limit in classical microscopy, the idea is to improve resolution by decreasing the wavelength of the probe. The de Broglie wavelength of an electron is given by

$$\lambda = \frac{hc}{\sqrt{E(2m_0c^2 + E)}} \ , \tag{2.11}$$

where λ is the wavelength of an electron, m_0 is the electron mass, E the energy, and c is the speed of light needed for the relativistic correction of fast-traveling electrons. In the case of a 60 keV electron, its wavelength is $\lambda = 0.05$ Å, enabling atomic resolution.

2.4.2 Electron lenses

We can manipulate electrons by using electric and/or magnetic fields. The Lorentz force describes the force on the electron passing through these fields:

$$\vec{F} = -q(\vec{E} + \vec{v} \times \vec{B}) \ , \tag{2.12}$$

where q is the charge of a particle (in this case, an electron charge e^-), $\vec{E}$ and $\vec{B}$ are the electric and magnetic fields, $\vec{v}$ is its velocity.

There are two lens types: an electrostatic and an electromagnetic lens. Electrostatic lenses have a high sensitivity to contamination and environmental impact. Therefore, we seldom use them for the manipulation of charged particle beams. Electromagnetic lenses consist of a coil. If an electron passes through the center of the lens, it does not experience any force. Off-center electrons deflect towards the middle in a helical path. We can describe those lenses as spherical lenses with their focal length proportional to $\left|\vec{B}\right|^2$.

2.4.3 Errors and corrections

In electron lens systems, different kinds of focusing errors can occur. In spherical aberration, the electron is more deflected the farther from the center it passes the lens. As electromagnetic lenses are cylindrical, this aberration is the most prominent. We call an aberration coma if a lens does not focus an off-axis beam at a single point. A nonspherical symmetric lens has multiple focal planes for different planes in the beam. Astigmatism is another typical aberration [explain] When chromatic aberration occurs, the lens does not have the same focal point for particles at different energies. There are two kinds of chromatic aberration. The longitudinal kind leads to different focal lengths, whereas the transversal focuses the beams at multiple points in the focal plane.

To correct those errors, we can design additional nonspherical lenses. The most common correction systems combine quadruple and octuple electromagnetic lenses [31]. This system cancels the aberration by shaping the electron beam to an elliptical form, correcting it, and making it symmetrical again. We need up to 76 independent power supplies to tune the correction lenses. In the case of the Nion UltraSTEM 100, we use four quadrupoles and three octopoles for correction. Therefore, we can correct aberrations up to the 5th order. The Nion UltraSTEM 100 also uses an automated algorithm to tune the lenses using an amorphous part of the sample [32]. However, correcting the first-order aberration or astigmatism is better done by hand.

2.4.4 Electron energy loss spectroscopy

When an electron interacts with a sample, inelastic scattering can occur. We can describe the state of this electron $|k\rangle$ as

$$|k\rangle = \frac{1}{L^{1/2}} e^{ikz} \phi(x, y) \ , \tag{2.13}$$

where $\phi(x, y)$ is the planar electron wave in the sample plane and $\frac{1}{L^{1/2}} e^{ikz}$ is the z component with impulse vector k of the electron.

We analyze the energy of this scattered electron using its impulse in the z-direction. A magnetic prism disperses the electrons based on their impulse using the Lorentz force (Equation 2.12). We then use a pixelated detector to obtain the energy-dispersive spectrum of a beam of electrons. The highest peak in the middle represents all non-scattered electrons. We call this the zero-loss peak (ZLP).

From an EELS analysis, we see energy lost or gained by the electrons. Therefore, we can analyze the elements, isotopes, phonon, and plasmon states. Using this technique, we can detect the vibrational states of the sample as well as temperature. Because of its contribution to the energy gain, we call this analysis electron energy gain spectroscopy (EEGS). The energy resolution is comparable to EELS but close to the ZLP width. The energy of typical phonon energy-gain states is approximately 0.1 eV and therefore needs a monochromated energy distribution in the probe and a high-resolution EELS detector. [33, 34]

2.5 Laser

A light amplification by stimulated emission of radiation (laser) source emits a coherent photon beam that has only one wavelength. All photons also have the same polarization and momentum and we can easily focus a laser onto a small spot, as there is no chromatic aberration and the spatial coherence results in an almost perfectly parallel beam. Locally, we obtain a high photon density and can heat this spot or enhance the probability of physical events such as photon-phonon coupling.

2.5.1 Theoretical description

A material with two energy levels E_0 and E_1, where $E_1 - E_0 = \Delta E = h\nu$ is an optical transition, can have spontaneous emission of a photon with the frequency ν. Then the electron relaxes to the ground state E_0. A photon with the energy ΔE can pump the medium and excite the electron into the state E_1.

Emission can also occur when a photon with an energy $h\nu$ passes by an electron in state E_1. The photon of this stimulated emission has the same properties and pulse as the stimulating photon. They are coherent. When more stimulated emission takes place, photons are absorbed to excite electrons. The light emitted is a coherent laser beam. If there are more electrons on the level E_1 than in the ground state, we call this a population inversion. This system is not in thermodynamical equilibrium and is, therefore, unstable without pumping.

In reality, most lasers work in a four-state system with the energy levels $E_0 < E_1 < E_2 < E_3$. We excite the electron state directly from the ground state E_0 to the level E_3. The relaxations E_3 to E_0 and E_1 to E_0 happen without any photon emission. They thermally pump the material. The relaxation E_2 to E_1 emits a photon with the energy $\Delta E_{21} = E_2 - E_1 = h\nu$. This process can happen spontaneously or be stimulated, therefore emitting laser radiation. For a population inversion, we pump the system with the energy $\Delta E_{03} = E_3 - E_0$.

2.5.2 Laser types

There are multiple methods to produce laser radiation, which mainly differ in their pumping and choice of laser medium. We can pump a laser using other lasers, electrons in diodes, or flash

lamps. The laser-active mediums can be solid, liquid, or gas. Commonly used liquid and gas lasers are dye or CO_2 lasers. The pumping laser is a diode laser and is, therefore, pumped by electrons. In our setup, we use a diode-pumped solid-state (DPSS) laser, a type of laser-pumped solid-state laser.

Diode lasers consist of semiconducting n- and p-type layers. Between those layers is a laser medium. A high voltage pumps this medium, resulting in spontaneous emission. If the pumping is sufficient, we achieve a population inversion. Spontaneously emitted photons lead to stimulated emission, finally leading to a laser beam [35].

We can use a diode laser to pump a solid-state laser medium. If we tune the pumping laser to the levels of the medium, we achieve a more efficient laser process than broadband flash lamps. Those lasers have narrow wavelengths because we pump them with the exact wavelength needed for the desired laser process. These lasers are more energy efficient, requiring less cooling and being more thermodynamically stable [36].

2.5.3 Laser modes

The intensity for transversal laser modes can be described by

$$I_{pl}(\rho, \phi) = I_0 \rho^l [L_p^l(\rho)]^2 \cos^2(l\phi) e^{-\rho} \ , \tag{2.14}$$

where L_p^l is the Laguerre polynomial with the order p and index l. We use the transverse electromagnetic mode (TEMM) to describe the modes of a cylindrical laser. In this thesis, the laser emits a $TEMM_{00}$ mode, and then the optical system maintains this mode.

2.5.4 Laser heating

Lasers can locally heat material by its absorption and scattering, thereby exiting phonon and plasmon modes with a high localized energy density. As lasers are spatially coherent, they can reach high photon densities on small spots, making the pumping more efficient than a non-coherent light source. We find a theoretical description for multilayer materials in [37].

2.6 Stimulated electron energy gain spectroscopy

As optical spectroscopy has an energy resolution below $0.1\,$meV and electron microscopy has a spatial resolution down to $0.1\,$nm, we can combine both techniques for optimal spatial and energy resolution. In a STEM, we can achieve this by pumping a sample with a laser with a low energy spread ($< 0.6\,$meV). Afterward, we probe the sample with an electron beam and analyze the interaction with EEGS/EELS. Therefore, we obtain a high spatial resolution and also, because of the laser, a high energy resolution. This combination of techniques was already proposed by Howie in 1999 [2].

Because electrons are fermions and photons are bosons, they cannot directly interact. However, in the presence of nanostructures, a second-order interaction is possible. A photon $|j\rangle$ with the energy $\hbar\omega_j$ can interact with the nanostructure and create an evanescent electromagnetic field. Then, we probe this field with an electron. This electron has the state

$$|k\rangle = \frac{1}{L^{1/2}} e^{ikz} \phi(x, y) \ , \tag{2.15}$$

where $\phi(x, y)$ is the planar electron wave in the sample plane and $\frac{1}{L^{1/2}} e^{ikz}$ is the z component with impulse vector k of the electron. We describe this interaction with the optically excited sample with the interaction Hamiltonian

$$\hat{H} = -\frac{ie\hbar}{mc} \hat{A} \cdot \nabla \ , \tag{2.16}$$

where $\hat{A}$ is the vector potential operator

$$\hat{A} = c \sum \sqrt{\frac{2\pi\hbar}{\omega_j}} \left[\hat{a}_j^\dagger f_j^*(r) + \hat{a}_j f_j(r) \right] \ . \tag{2.17}$$

Here $f_j(r)$ are the electric field eigenfunctions created by photon pumping, and ω_j are the photon state frequencies. They are a characteristic of the nanostructure. A photon ($|j\rangle$) pumps a nanostructure and therefore is consumed ($|0\rangle$). The probing electron changes the state $|k_i\rangle$ to $|k_f\rangle$ described by

$$\langle k_f | \langle j | \hat{H} | 0 \rangle | k_i \rangle \ . \tag{2.18}$$

The probability for this interaction is

$$P_j = \frac{2\pi L}{\hbar^2 v} \sum_{k_f} \left| \langle k_f | \langle j | \hat{H} | 0 \rangle | k_i \rangle \right|^2 \delta(\omega - qv) \ , \tag{2.19}$$

leading to a total probability for stimulated electron energy gain spectroscopy (sEEGS) to happen of

$$P_{\mathrm{sEEGS}}(\omega) = \left(\frac{e}{\hbar\omega} \right)^2 \left| dz E_z(R_e, z) e^{-i\omega z/v} \right|^2 \ . \tag{2.20}$$

This means that according to [34] a continues wave laser with a power density of 10^6 W cm^{-2} has a probability compared to the EELS making sEEGS feasible to be detected [38–40].

Previous studies have shown sEEGS for a pulsed laser with continuous electron probing to be measurable. The laser and the EELS detector were synchronized to enhance the signal-to-noise ratio [39].

2.7 Sample cleaning

The emergence of low-dimensional materials and methods for atomic resolution resulted in a need for atomically clean surfaces. Many different cleaning techniques were and are used to achieve this. Most of those techniques are *ex-situ*, like baking and chemical cleaning. Seldom *in-situ* or *pre-situ* methods are used to avoid exposing the sample to ambient conditions between cleaning and characterization and keep them in a vacuum. We first give a broad overview of existing cleaning techniques, further understanding the challenges and prospects of sample cleaning.

2.7.1 Prospects and challenges

Contamination of samples hinders atomic resolution in microscopy techniques. Also, it changes the sample's electrical and mechanical properties [41].

There have been a few studies on identifying the contamination of graphene and other 2D materials. The most common contamination reported is poly methyl methacrylate (PMMA) caused by sample transfer [42]. Also, the handling of the sample can induce hydrocarbon contamination. Airborne hydrocarbons and hydrocarbons from plastic sample trays have been reported to contaminate the sample [43]. The length of these hydrocarbons is between 20 and 26 C atoms and there were no functional groups reported [44]. Other studies found contamination like ligands and impurities such as Si on samples.

Due to the use of acidic chemicals or high power in heating and other physical processes, the cleaning process can alter the sample. Also, when cleaning initial contamination, the process can induce additional contamination.

Using acidic chemicals in etching processes has been reported to induce various defects and contamination, especially on more delicate samples [45]. Metal nanoparticles from the catalyst used in CVD processes can form upon etching [46], as well as ligands [47]. Etching in silicate glassware can induce Si defects in graphene [48].

High power in physical cleaning processes such as heating can anneal the material and destroy desired doping [47, 49]. Plasma treatment can induce defects in the material and also change its properties [50–52]. Also, electron beam-induced recontamination and graphitization of amorphous carbon on the sample has been reported [49]. As 2D materials are atomically thin, every contamination or altering of the material can change its properties. Optical properties of 2D materials are influenced by surface contamination and charged impurities [42] as they alter the phonon and plasmon structure. These changes in the structure induced by contamination also change the electric properties of the material [53] such as conductivity [54]. Mechanical properties also change with contamination or changes in the sample, for instance, the wettability of graphene [43].

2.7.2 Producing cleaner samples

As some of the contamination arises from the sample production and transfer itself, a first approach is to optimize these processes towards clean samples.

The use of O_2 [55] or H_2 [46]-bubbling instead of highly acidic solvents reduces the contamination by metal nanoparticles. H_2O_2 and $K_6S_2O_8$ with graphene/Cu electrodes in solution are used to intercalate between the catalyst and the graphene. As respectively H_2 or O_2 bubbles emerge from the process, it is called bubbling. This method also reduces the wear of the catalyst [55].

Not using transfer methods with a contaminant such as PMMA is favorable and enhances sample cleanness. One reported alternative is antherance [56].

2.7.3 Chemical cleaning

To achieve contamination-free areas on the sample, we can use wet and dry chemical processes to clean the sample. The most common dry chemical cleaning is heating the sample in activated carbon. Wet chemical processes clean carbon and hydrocarbon contamination using solvents and acids. Etching of the contamination achieves reportedly clean surfaces [57]. We can enhance these processes by adding a catalyst such as Pt.

Chemical cleaning can remove hydrocarbon contamination and metal nanoparticles but has also been reported to damage the sample [57].

Solvating lipophilic hydrocarbons in isopropyl alcohol (IPA) and acetone can clean samples. These solvents are not very effective concerning atomically clean surfaces but can remove rough contamination for further cleaning [53].

Clean samples can be achieved by using standard, widely available chemicals to etch away the contamination. This etching can be quite effective in cleaning samples from hydrocarbons and PMMA. As etching agents $FeCl_3$ [57], $(NH_4)_2S_2O_8$ [57], O_3 [43], and NaOH can be used. However, these methods still leave some residues on the sample, reportedly amorphous carbon, metal nanoparticles, and ligands.

Various studies reported good cleaning results using *ex-situ* cleaning with dry chemical cleaning. For active carbon treatment, they show a cleanness of the sample at 65%. Reports show the migration of hydrocarbons on the sample during scanning electron microscope (SEM) investigation, thus contaminating it again. Previous studies propose that the active carbon cleaning and the use of a Pt catalyst only clean the PMMA from the sample transfer [56].

2.7.4 Physical cleaning

In contrast to chemical cleaning, physical cleaning makes use of heat, ionization, and mechanical strategies such as plasma and laser cleaning or cleaning with an atom-force microscope (AFM). Physical cleaning can be used standalone or together with chemical cleaning procedures.

We can clean stable structures such as graphene *in-situ* using an AFM. This cleaning process does not chemically interfere with the sample but cleans small areas. The sample is cleaned by bringing the sample into contact with the AFM tip and wiping over the sample surface [49, 58, 59].

To clean a sample, we can shower it with a plasma beam. Widely used gasses in sample cleaning are Ar and H_2. The radicals in the plasma beam chemically interact with the contamination on the sample, breaking especially long hydrocarbons and destroying metal nanoparticles. Because of the high energies in the plasma and its chemical activity, it can change the structure of the sample and its chemical composition, also inducing defects or annealing them. The damage and cleaning effects depend on the chemical composition of the plasma. O_2 plasma has been reported to be more destructive [47].

Sample contamination can also be removed by heating the sample. We can apply this in Ar atmosphere or vacuum [60]. During heating, solvents or activated carbon can be added to the process [61]. We can use a heating chip enabling this technique for *in-situ* cleaning. Because of the need for a special chip, this does not work with out-of-the-box samples [60]. During heating, graphene can also react with the contamination on the sample, which binds it and anneals itself [61].

2.7.5 Laser cleaning

Using a laser for cleaning was developed for *pre-situ* cleaning in a vacuum. Illuminating the sample with a laser can atomically clean selected areas of the sample on the order of tens of micrometers [3]. We deploy this method as an *in-situ* method in this work, and its cleaning capabilities are further studied.

Table 2.1: Overview and comparison of already established chemical cleaning methods

	Method	Advantages	Disadvantages
Chemical cleaning	Pt catalyst [56]	▪ Removes PMMA and other hydrocarbons [56] ▪ Cleans anthracene from a deposit	▪ Contamination buildup during SEM imaging ▪ needs an external catalyst
	Activated carbon [56, 62]	▪ Noninvasive ▪ Simple to use ▪ Cleanness up to 95%	▪ No cleaning of multilayer ▪ Only tested on graphene ▪ Air exposure after cleaning
	Methanol [63]	▪ Defect-free graphene ▪ Eliminates residuals from acetone transfer	▪ Not storage stable ▪ *Ex-situ* method
	Base washing [64]	▪ Cleaning of dirt on graphene oxide ▪ No residual hydrogen (use NaOH in process)	▪ Reducing of O_2 ▪ Wet process
	Standart solvents [53]	▪ Commercially available ▪ Chlorophorm can dissolve PMMA [53] ▪ Chloroform can improve electric properties of graphene [53]	▪ Not able to remove Acetone and pyrolytic graphite residue [65]
	Etching [57]	▪ Standard methods ▪ Cleaning on transfer	▪ Metallic residues ▪ Amorphous carbon building ▪ Destruction of catalyst [46]
	Electrochemical delamination [46, 57]	▪ Clean graphene ▪ Recyclable catalyst	▪ PMMA residues ▪ Metal nanoparticles on sample
	O_2 bubbling [57]	▪ Relative clean graphene ▪ Only water needed	▪ Cu residue ▪ PMMA residue ▪ $Cu - N - O$ phase on sample

Table 2.2: Overview and comparison of already established combination physical and chemical cleaning methods

	Method	Advantages	Disadvantages
Chemical + physical cleaning	e^--beam + heating + water [66]	▪ *In-situ* method ▪ 80% cleaning of PMMA	▪ Water vapor in the column ▪ Chemical etching and radicals in column ▪ Large sample surface affected
	Heating in Ar/H_2 atmosphere [65]	▪ Atomical cleaning ▪ Cleaning of pyrolytic carbon residues ▪ *In-situ* method ▪ Complete removal of surface impurities	▪ Need of atmospheric control
	UV + O_3 annealing [43]	▪ Cleans some hydrocarbons	▪ Not very clean surface

Table 2.3: Overview and comparison of already established physical cleaning methods

	Method	Advantages	Disadvantages
Physical cleaning	AFM cleaning [58, 59]	▪ Atomical clean surfaces ▪ No sample damage ▪ Double-layer cleaning [59]	▪ AFM needed in vacuum ▪ Single side only
	Heating [47, 53, 60, 61]	▪ Can be deployed in cryo-TEM ▪ Large clean areas ▪ Heating and H_2/Ar desolves some PMMA ▪ Effective for hydrocarbons [47] ▪ Up to $500\,°C$ no destruction of graphene [53]	▪ Special sample needed ▪ Electrical contact on sample needed ▪ Still some PMMA on the surface ▪ Weak cleaning for ligands [47] ▪ Structure changes [47]

	Plasma [41, 51, 52, 67, 68]	▪ *Pre-situ* is possible ▪ No residual chemicals ▪ Vacuum capable ▪ Cleaning of polymeric contamination [41] ▪ Graphene has an energy barrier for H_2 plasma cleaning [41] ▪ After annealing: Pristine graphene ▪ Low density Ar plasma can clean few-layer graphene devices [51] ▪ Cl plasma can clean SiO nanoparticles [68]	▪ Induces defects [50, 51] ▪ Sample destruction [50, 51] ▪ After annealing: defects vanish ▪ No *in-situ* ▪ O_2 plasma can react with sample [47] ▪ H plasma can cross the graphene barrier and damage or anneal [52] ▪ H plasma can induce liftoff of graphene from SiO_2 surfaces
	Beam showering [47]	▪ Clean areas ▪ Effective for ligands	▪ Limited in time ▪ Small areas ▪ Fast recontamination
	Pre-situ laser [3]	▪ *In-situ* is possible ▪ No residual chemicals ▪ Vacuum capable	▪ Sample destruction

3 Methods

In this thesis, we develop and introduce an *in-situ* laser system for the nion UltraSTEM 100 as a part of the CANVAS system. We use the optical microscope Infinity K2 DistaMax to focus a laser onto a sample in the STEM. To achieve this, we characterize the optical microscope, design samples for testing in the STEM, and alignment. With this setup, we perform a cleaning study and analyze the data with an automated algorithm.

3.1 Characterization of the optical system

3.1.1 Untouched optical microscope

We characterize the optical microscope to evaluate its feasibility and rough spot size for the intended use as a laser-focusing device. The microscope is a Infinity K2 DistaMax equipped with the CF1 far-field objective, CF-Tube, 50/50 beam splitter, and a K2 CentriTel™ focuser described in [69, p. 20]. We use the optical microscope in the configuration shown in Figure 3.1. The nominal resolution of this system is $6\,\mu$m at a working distance of $34\,$cm [69].

For a first approach to estimate the spot size achieved by the optical microscope without any additional optics, we use a ThorLabs CPS532 DPSS laser. The laser has a wavelength of $532\,$nm at $4.5\,$mW and an aperture of $4.8\,$mm [70]. A webcam chip without any optics installed measures the laser spot size at the focus point, as shown in Figure 3.1.

3.1.2 Measuring single lenses in the microscope

We characterize the optical microscope Infinity K2 DistaMax by measuring each lens individually. Also, we estimate the lenses' mechanical position using a caliper with $100\,\mu$m precision. Therefore, we completely disassemble and characterize the microscope.

An experimental setup, as shown in Figure 3.2, measures the lenses. First, we collimate a white light source with a black-body radiation temperature of $2750\,$K. This light probes sample lenses. As a detector, we use a $3\,$mm by $2\,$mm webcam chip, which is mounted on a 3-axis stage to improve the field of view as well as enable scanning along the optical axis. At each z-position on this axis, multiple images are stored in a scanning pattern to capture the whole light spot at this position.

The detector stages consist of two Physik Instrumente M-403-626 in the horizontal plane and a Thorlabs MTS50-Z8 in the vertical axis. A Python script takes care of the data acquisition

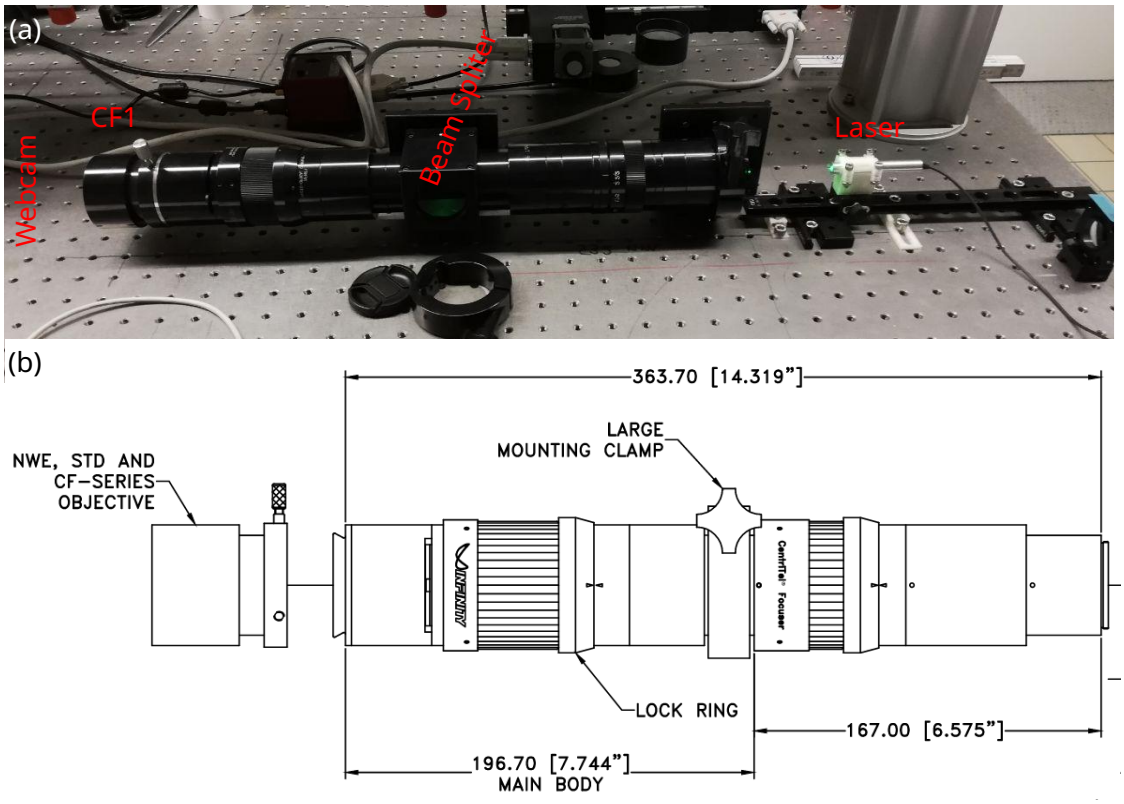

Figure 3.1: (a) First hands-on experiments on the optical microscope K2 DistaMax in the Laser Lab. We show a mirrored image for better understanding. (b) Technical drawing of a similar setup by the manufacturer [69].

and the stage control. The script saves the image as capxyz.png. The sample holder comprises spare parts from the optical microscope mounted on a 2-axis rotary stage for alignment. The probe light beam passes the lens from both sides, one after another.

3.2 Scanning transmission electron microscope

Scanning transmission electron microscope (STEM) images a field of view by scanning a small probe over the site of interest. The detector intensity defines the value of each pixel in the image.

3.2.1 Nion UltraSTEM 100

The Nion UltraSTEM 100 is a dedicated scanning-transmission electron microscope with probe correction. This microscope emits electrons using a cold-field emission gun. However, they are not monochromated, resulting in a broader energy spread. The microscope has two annular dark-field detectors, one for medium angles (MAADF) and the other for higher angles (HAADF). An electron energy loss/gain spectroscopy (EELS/EEGS) detector analyses unscattered electrons [32].

The Nion microscope comes with a cold-field emission gun. This gun accelerates the electrons

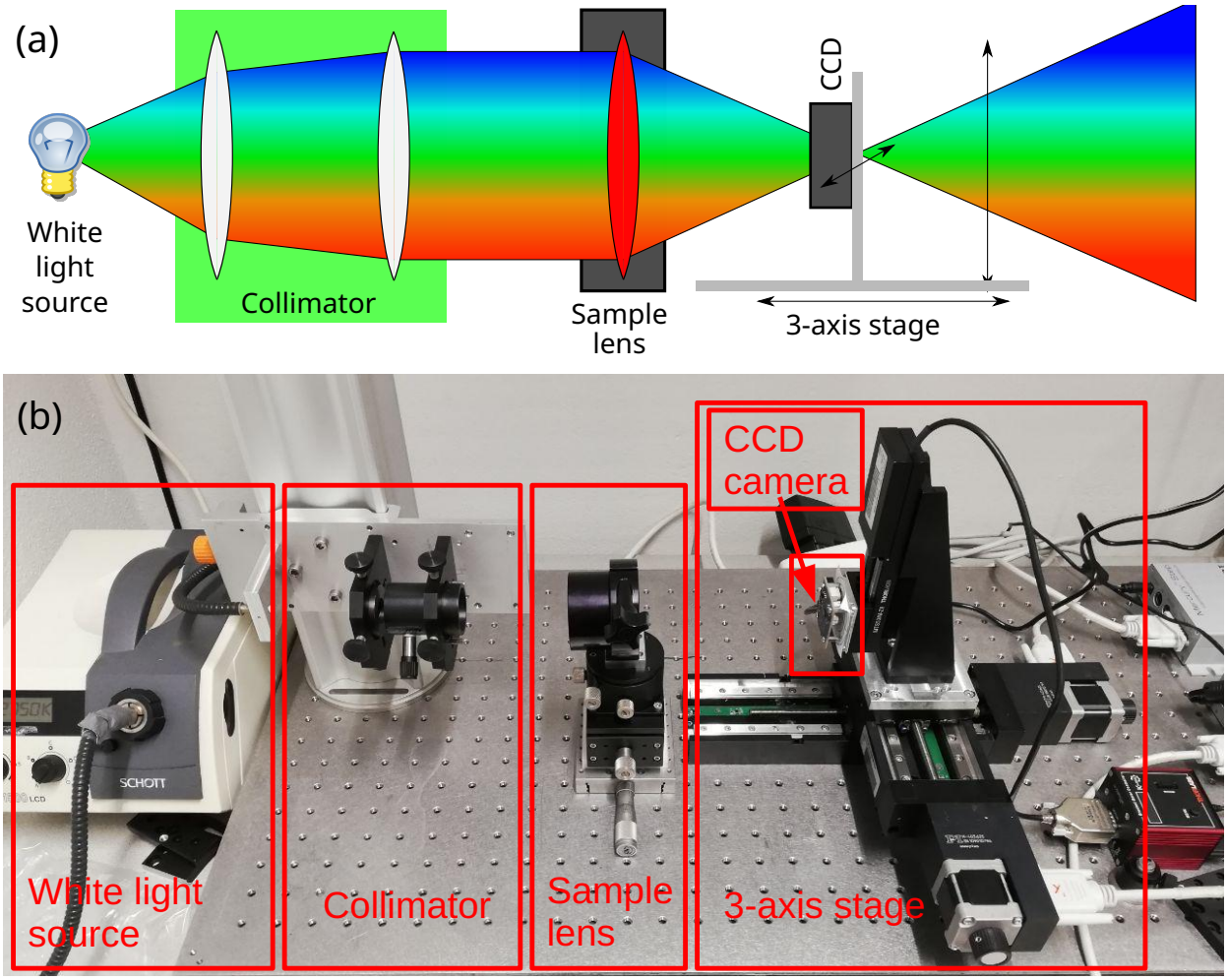

Figure 3.2: (a) Schematic drawing of lens measurements: a collimated white light source using black body radiation at $2750\,\mathrm{K}$ probes a lens of the optical microscope. A 3D-scanning charge-coupled device (CCD) webcam then measures the interacting beam. (b) Real-life experiment: white light is collimated to probe a sample lens. We place the detector on a stage assembly with a range of $150 \times 150 \times 50$ mm^3.

with voltages of $(40 - 100)$ kV. A cold-field emission gun does not need to be heated to extract electrons. A bias voltage extracts the electrons from an atomically sharp tip before the acceleration voltage is applied. A cold-field emission gun has a low thermal energy spread, resulting in a smaller energy spread overall.

The Nion UltraSTEM 100 focuses an electron beam up to a diameter of 1 Å on the sample. An array of multiple magnetic lenses in Ultra High Vacuum (UHV) shapes the electron beam. The scanning procedure is controlled and synchronized with the Nion PC. Therefore, it can calculate images from integral detector data. A variable electromagnet controls the beam scanning the sample [32, 71].

A widened electron beam creates TEM-like imaging with a wider field of view, which makes navigation on the sample easier. Also, in this mode, we see and measure the evaporation effects of the laser illumination.

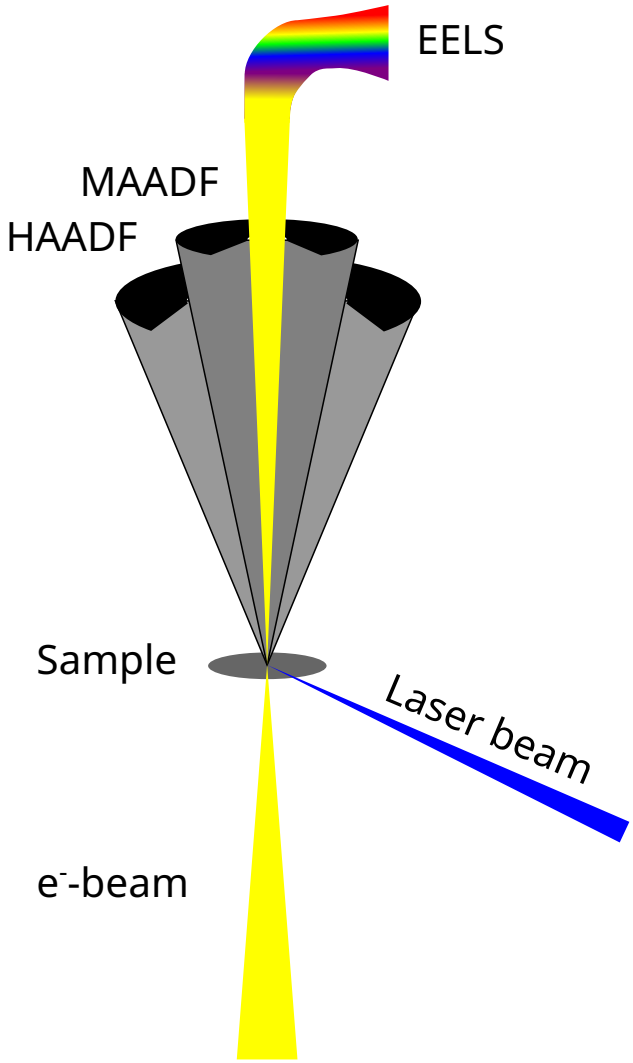

Figure 3.3: Schematic representation of beam paths in STEM: The sharply focused electron beam coincides with the focused laser beam at the sample. Afterward, a HAADF and a MAADF detectors measure the scattered electrons. The electron energy loss spectrometer analyzes the inelastically scattered electrons.

3.2.2 Aberration correction

Magnetic lenses limit electron microscopy due to high spherical and other aberrations, which are discussed in 2.4.3 in detail. Advances in computing power enabled aberration correction of magnetic lenses. To correct aberrations, the STEM uses nonspherical lenses.

A scanning microscope corrects the aberrations before interacting with the sample to keep the focal point of the probe small. This enables 1 Å resolution. By individual tuning aspheric lenses such as multi-pole magnets, we correct aberrations up to the fifth order.

Nion supplies an automatic correction algorithm with their Nion UltraSTEM series. This algorithm can automatically correct aberrations up to the fifth order. We use this automation to correct our probe. First, we measure the error of the lowest order and then apply the suggested correction. When the error is minimized, we proceed with a higher order correction. High-order

corrections can alter the lower-order corrections. Therefore, we start correcting from the lower order again, and iterate.

Astigmatism is a first order term that the algorithm fails to correct. However, we do this by hand as a trained operator is more efficient with this type of error. Starting at near-atomic resolution, we look at asymmetries in the image or its Fourier transformation. We then tweak the correction parameters until we reach optimal resolution.

3.2.3 Annular dark-field detectors

When electrons interact with a sample, they scatter at an angle. Annular dark-field detectors (ADF) detect electrons scattered from a sample. These integral detectors have a hole in the middle, thus are annular detectors. Samples scatter probe electrons at different angles depending on their chemical composition and atom structure. Depending on the angle of the detector placement, we call them medium or high-angle ADF (MAADF, HAADF).

The first annular detector after the sample holder is the high-angle annular dark-field (HAADF) as pictured in Figure 3.3. The HAADF detects strongly scattered electrons, like the one scattered by heavy nuclei at angles of $(80\text{–}300)$ mrad.

Farther away from the sample in the column, there is the medium-angle annular dark-field (MAADF) detector. It detects less strongly scattered electrons from the sample at angles of $(60\text{–}200)$ mrad. This detector is well suited to image graphene samples. We use the MAADF detector to determine the cleaning effect on graphene samples and detect clean areas.

3.2.4 Bright-field detector

We can place a scientific CCD camera between the sample and ADF detectors to emulate a TEM mode. As the laser evaporates material from the sample there are visible contrast between the laser affected area and the plain sample in the CCD image. This can be used to fine align the laser and by measuring the evaporated area we get an estimate of the laser spot size on the sample (Section 4.1.4 and 4.1.8).

3.2.5 Electron energy-loss and -gain spectroscopy

Electron energy-loss or -gain spectroscopy sorts the electrons by energy. The Lorentz force in a magnetic prism deflects the electrons according to their pulse in z-direction. Those energy-dispersed electrons now hit a phosphorous scintillator, which converts them to light. Thereafter, an Andor intensified charge-coupled device (iCCD) detects the energy spread of the electrons. However, as the phosphorous layer works by luminescence, it is prone to long-lasting afterglow at regions of high electron intensities, such as the zero-loss peak. We can shift the beam to avoid afterglow on the scintillator. In this thesis, we do this after every measurement. Alternatively, one can also wait for the afterglow to subside.

The Nion UltraSTEM connects the EELS system with the scanning. Therefore, we can create EELS maps in addition to electron energy loss point spectra.

3.3 CANVAS system

Previous developments in sample handling to avoid exposure to ambient conditions and further contamination of the sample led to the development of the controlled alteration of nanomaterials in vacuum down to the atomic scale (CANVAS) system. It allows Sample transfer in UHV between different experiments like a *pre-situ* laser cleaning device. The CANVAS system also enables in-vacuum storage of samples over an extended period. Therefore, we can perform cleaning studies without heavily contaminating the samples again during storage [72].

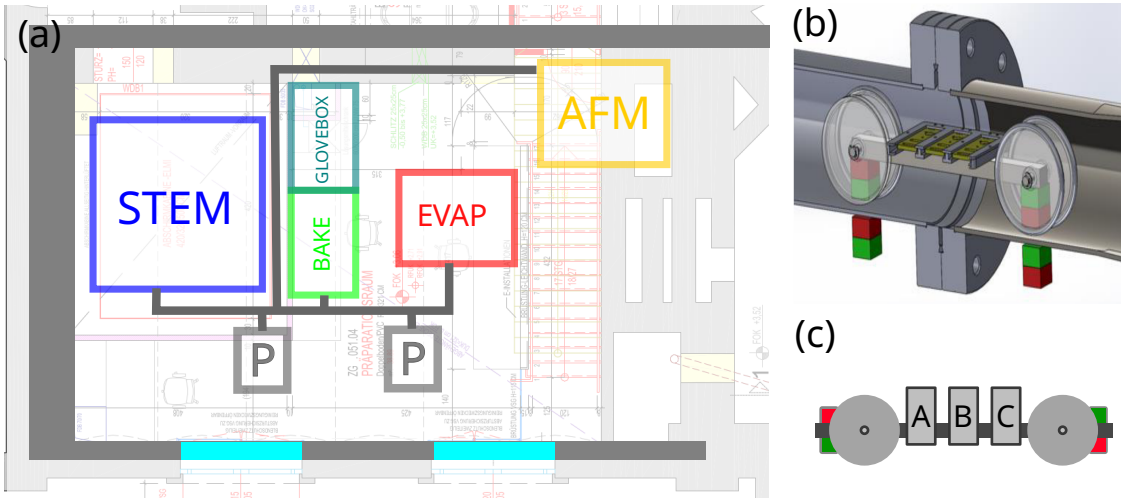

Figure 3.4: CANVAS-system: (a) schematic floor plan of CANVAS with attached devices. (b) and (c): "car" for sample transfer in a vacuum, where (b) is a CAD render of the car in the system and (c) is a schematic drawing of the car with its sample holders A, B, and C. The images (a) and (b) are taken with permission from [72].

In this thesis, we develop an *in-situ* laser system in addition to the previously existing CANVAS system. The laser at the STEM is part of CANVAS. We use the STEM, bake, and the parking garages (P) as described Figure 3.4. We use those devices to minimize initial contamination and recontamination during our experiments and storage of our samples.

3.3.1 Vacuum system

The STEM is attached to a UHV system, which enables sample transfer inside a vacuum (10^{-9} mbar) between experiments, storage areas, and the STEM. Each sample is baked at $150\,^{\circ}$C for 12 hours in an argon atmosphere when being transferred to the vacuum system. Once the sample is in the system, we don't need to remove it from the UHV at any point, as the system has storage capabilities for keeping samples in UHV conditions.

The samples inside the system can be moved in UHV by magnetic coupling and specially designed carriers ("cars") and transferred between different experiments and UHV sample storage. Also, we can exchange samples in the same vacuum conditions within minutes [72]. All samples used are in the vacuum system during all experiments.

3.3.2 Vacuum transfer system

Before we insert a new sample into the CANVAS system, we have to clean it. Sample contamination like hydrocarbons and gases like O_2 affect vacuum quality. We can use activated carbon to clean the sample ex-situ. Additionally, we also ensure a clean workflow when handling the sample. The sample must only have contact with vacuum-grade clean tweezers and oil-free aluminum foil. A load lock bakes the fresh sample at $150\,^{\circ}$C in Ar atmosphere.

Specially designed "cars" move the samples in the vacuum system. Those "cars" can move through the pipes controlled from outside using strong magnets coupling to the front and back of the "cars".

Grippers load the sample from a car to a device or experiment. This gripper can remove a puck from and place it on a stage or into an experiment.

We can store samples in so-called "parking garages" under UHV conditions. Every car is accessible independently of storing order because we store them in a star-shaped pattern.

3.3.3 *Pre-situ* laser cleaning

The CANVAS system can laser-clean a sample once in a vacuum. Therefore, we place the sample in the so-called "target chamber" where a diode laser points at the sample to clean it. This process is not precise and, the sample needs to be transferred to the STEM for verification [3].

3.4 Samples

3.4.1 Bare quantifoil

We firstly use a standard support grid R 1/1 from Quantifoil. This grid is an amorphous carbon film with a holey pattern suspended on a standard gold TEM grid with a $3\,$mm diameter. The holes in the Quantifoil layer are $1\,$µm in diameter and have a periodicity of $2\,$µm.

Bare Quantifoil support films without graphene on top of them have a significant lower thermal conductivity compared to graphene (Section 2.2). Therefore, we use them to measure the spot size of a laser. We use the hole sizes to calibrate the CCD camera of the nion UltraSTEM 100.

3.4.2 Graphene

As a standard for testing and proof of concept studies, we use ready-to-use single-layer graphene samples on TEM grids manufactured by Graphenea. Those samples have a high uniformity and monolayer selectivity.

Graphenea produces its graphene with chemical vapour deposition (CVD). This process produces relatively big graphene flakes with small numbers of defects and grain boundaries. The graphene sheets are cleaned and transferred onto a Quantifoil amorphous carbon support layer. The support layer has a hole size of $2.5\,\mu m$ with a periodicity of $5\,\mu m$.

3.4.3 Carbon nanotubes

CNTs described in Section 2.2.2 can have multiple wall sizes and lengths. This study primarily uses DWCNT sourced from the nanomaterials group (NMG) at Aalto University. Those networks are then transferred onto different support grids and sample holders as described in Section 3.4.5 and Section 3.4.4.

There are two techniques for sample transfer. We call them wet and dry transfer. For wet transfer, we place a CNT network deposited on a paper filter face down on top of a support structure. A micro-positioning tool combined with an Olympus BX51WI optical microscope brings the CNT network into position. A single drop of IPA transfers the CNT network to the support structure.

For dry transfer, the CNT network is also placed on top of a support structure and pressed with as low pressure as possible onto the support structure. This process can destroy some delicate support structures but is faster and easier than the wet transfer.

3.4.4 Thermal stable sample

We needed a sample with high thermal stability because of the high laser intensities used in stimulated electron energy gain spectroscopy. The Quantifoil samples used previously have shown evaporation of the Quantifoil support substrate already for small laser intensities. The laser even can damage silicon-nitride-supported samples.

To address these necessities, we produced a thermally stable sample. The support grid consists of a Double-Walled Carbon Nanotube network because it has high thermal and mechanical stability. We transfer the DWCNT network onto a copper sample holder with a $400\,\mu m$ thick hole in the middle. On top of this support "grid", a CVD-grown single-layer graphene sheet was wet-transferred.

3.4.5 Electrical alignment sample

The sample uses a Wildfire D6 Nano-Chip XT1200 heating chip from DENSsolutions. This chip has a calibrated heating curve and a radially symmetric coil for heating as well as slits in

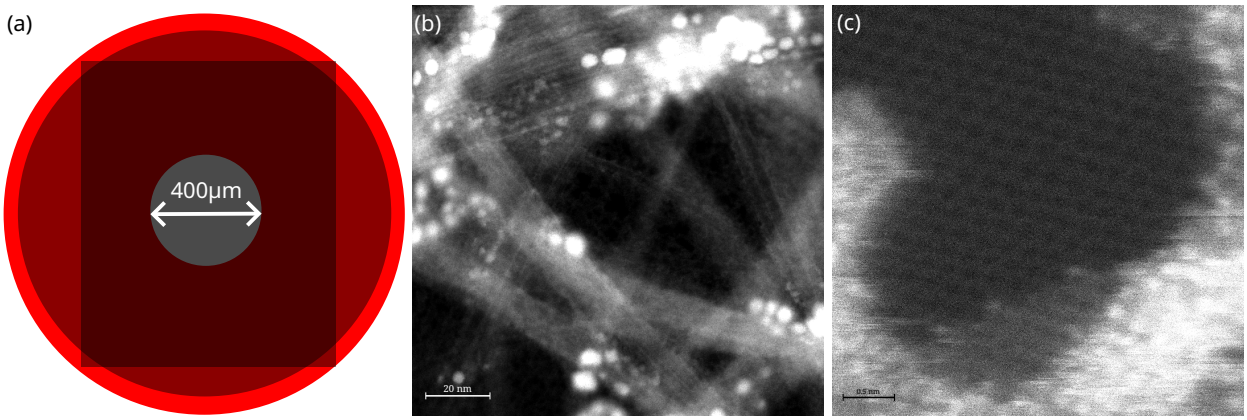

Figure 3.5: Single-layer graphene suspended on double-walled carbon nanotubes. (a) Schematic sketch of the sample: the red circle is the copper sample holder. (b) Zoom into the sample: the bright lines are the DWCNT network between the graphene lattice. (c) Atomic resolution of the graphene lattice suspended onto the DWCNT network.

the membrane for electron microscopy. Figure 3.6 shows the heating calibration curve and the geometry of the alignment sample.

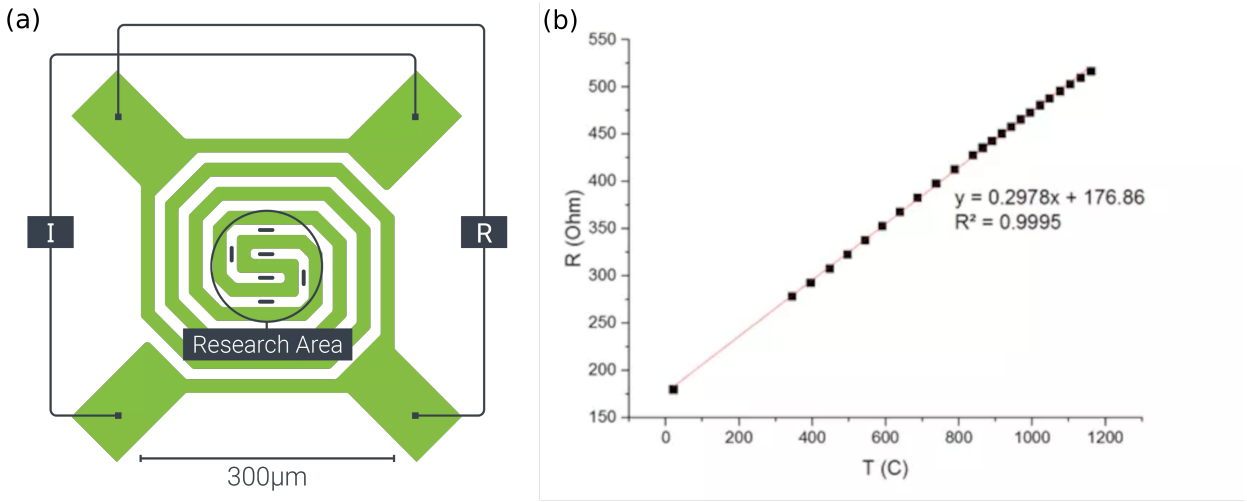

Figure 3.6: Specification of the heating-chip XT1200 used for laser alignment: (a) In the geometry of the chip, you can see the radial symmetric coil and the slits in the membrane for transmission electron microscopy from [73]. (b) Heat-resistance calibration curve of the chip with a 4-point measurement from [74].

The alignment sample has to withstand long and high laser illumination while enabling us to detect the zero defocus point. For the electrical alignment using a 4-point resistance measurement, we transfer a DWCNT network to a Nano-Chip. The transfer is made in wet conditions using isopropanol and a micropositioner with an optical microscope. Finally, we glue the Nano-Chip, with the DWCNT network, to a titanium support and wire-bond it to an adapter PCB for use in a Nion electrical cartridge.

3.4.6 *Ex-situ* cleaning before vacuum

Additional cleaning before being transferred into the vacuum system helps to ensure cleaner samples. As a wet cleaning method, we submerge the sample into IPA and acetone to remove some hydrocarbon contamination. Additionally, we cover the sample in activated carbon and bake them in a small household oven for $30\,\mathrm{min}$, resembling a dry cleaning method. We use these processes to achieve consistency in sample contamination.

3.4.7 Sample transfer

We additionally bake every sample when it enters the vacuum system. Before we transfer the sample to the rest of the CANVAS system, we first need to bake it in Ar atmosphere at $150\,^{\circ}$C for at least $12\,$h. Afterward, the car can proceed into the system via a double gate.

If we prepare the sample for use with the Nion magazine, we need to bake the sample in an Ar atmosphere. A proprietary baking station supplied by Nion fits the magazines and performs the baking. The bake should take at least $6\,$h at $160\,^{\circ}$C. We exchange the magazines at approximately $70\,^{\circ}$C to reduce contamination.

3.5 In-situ laser system

In this thesis, the main goal is to design and characterize an in-situ laser system for the Nion UltraSTEM 100 to allow laser illumination of samples during STEM imaging.

3.5.1 Planned optical path

We plan the optics of the laser system to enable the simultaneous coupling of multiple lasers with different parameters. The chosen laser beam then passes additional optics for advanced beam shaping before entering the optical microscope optimized for imaging. To couple in the beam, two 45° mirrors on an X-Y-stage are used for alignment into the microscope. The laser then hits the sample at an angle of approximately 20°, determined by the fixed viewport installed on the column.

To achieve pulse length as low as $100\,\mu$s, a double curtain shutter assembly from the digital single-lens reflex (DSLR) camera Canon EOS 60D is used. This shutter assembly is controlled using a Raspberry Pi and an additional circuit board to tension and ignite the shutter. The actual opening time of the shutter can be measured using a photoelectric barrier made from an light emitting diode (LED) and a photodiode. A RedPitaya single board computer with integrated field programmable gate array (FPGA) measures the shutter speed using its oscilloscope function.

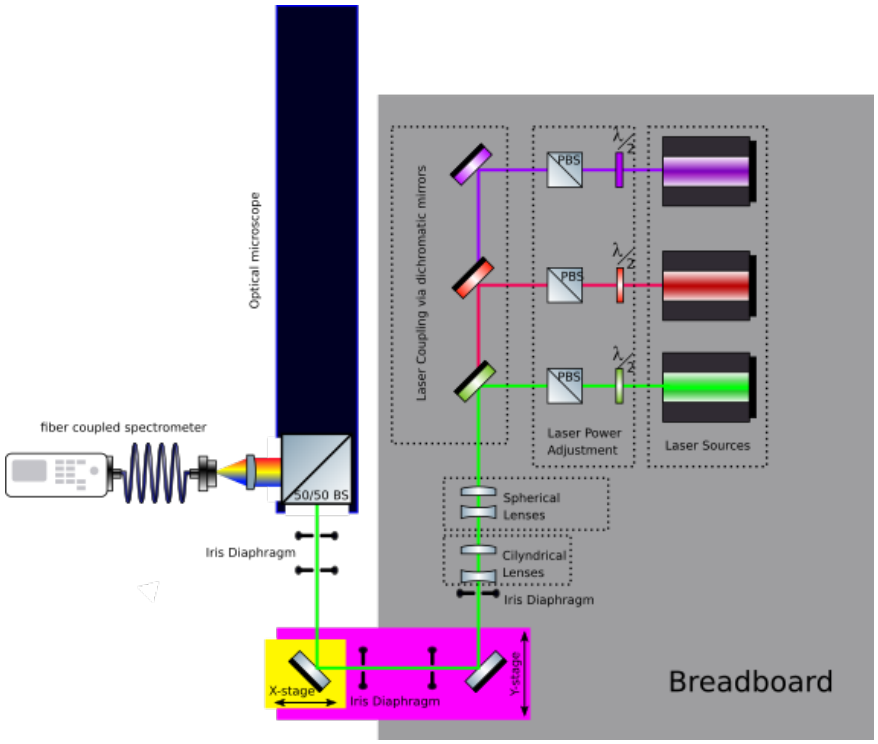

Figure 3.7: Laser setup as proposed considers different wavelengths, for which an optical table provides the necessary mounting. The design goal of the system was to couple out the light from the STEM for optical spectroscopy. We use free-space coupling to ensure constant laser modes at different wavelengths.

3.5.2 Coupling considerations

The design goal of the in-situ laser system is to focus a laser beam on a sample inside the STEM column. We keep the focus diameter small to ensure that all laser-induced effects and damage do not affect aloof sample regions. For the focusing of the laser, we use a long-range microscope Infinity K2DistaMax (Section 3.1). The laser couples into this microscope via a free-space coupler, maintaining the TEMM_{00} mode of the lasers at different wavelengths. Before coupling in the laser, a lens assembly narrows the beam diameter for a smaller spot on the sample. Additional irises help us with the alignment.

For the initial setup, a Cobolt 04-01 Blues DPSS with a central wavelength of (473 ± 0.1)nm [75] is chosen. This laser has a high enough single photon energy to be detected by EEGS experiments. This laser also comes with a stable and well-documented [75] TEMM_{00} mode until $50\,$mW and a maximum power of $80\,$mW.

3.5.3 Mounting and mechanics

A carefully designed mechanical mounting and shielding achieves the precision and stability needed for the system. The mounting of the optical microscope consists of a 2-angle double-bearing gimbal. This gimbal improves stability while allowing angle alignments. The entire system is mounted on an optical table with 40×40 mm^2 Al-profiles, as they deliver the most

design flexibility. The modular design of the laser system simplifies its maintenance. We also mount this module on the same isolated air table as the electron microscope. Therefore, we decouple the system from external vibrations and remove the need to couple two mechanically isolated and separated systems.

To ensure alignment stability and keep the system from accidental user interference, a shield made of an Al-sheet is mounted to protect the optical microscope and its alignment. The sheet itself is isolated from the laser system with rubber dampers.

3.5.4 In-situ laser cleaning

The primary purpose of the laser system is to clean contaminated materials. With the design of this system, we can clean samples in situ, similar to the cleaning discussed in [3]. This new system will affect smaller areas and can be more precisely aligned. Therefore, we can clean more delicate samples. This thesis discusses the cleaning capabilities and optical characteristics in detail (Section 3.6).

3.5.5 Alignment of the system

The planned spot size is estimated to be approximately $20\,\mu m$. Therefore, the laser system has to implement alignment methods.

To achieve this, we implement two XY micrometer stages in the setup. One is a custom translation stage, seated at the coupling to the optical microscope. The other one manipulates the angle of the optical microscope.

A camera attaches to the beam splitter, and optical clues help coarse align the optical microscope. For a more precise alignment, we design a custom electrical alignment sample (Section 3.4.5). As the electrical resistance of the sample changes with heat, we can use a 4-point measurement to maximize the resistance due to the alignment of the laser system. We can further use a sacrificial bare Quantifoil sample to get the alignment to a micrometer precision. The damage of the carbon foil by the laser gives the feedback necessary to align the laser step by step.

3.5.6 Controlling the system

An RS-232 interface connects the laser controller to the system controller. We run the laser controller in an original equipment manufacturer (OEM) mode to obtain complete control over the laser. A specially designed board controls the shutter with $3.3\,V$ transistor-transistor logic (TTL) signals. We connect those interfaces to a Raspberry Pi single-board computer. The Raspberry Pi provides network application programing interface (API)s to enable external configuration and control as described in Section 4.1.7. We also integrate a graphical user interface (GUI) as a Nion Swift plug-in for improved usability.

3.5.7 Spot characterization on the sample

The evaporation effect of heated Quantifoil allows an estimate of the full-width half-maximum (FWHM) size of the laser spot hitting the sample. Quantifoil has a lower thermal conductivity compared to other sample materials like graphene. The visible evaporation is mainly due to direct laser heating. We illuminate the sample with the laser for different durations. The total energy of the laser illumination is then compared with the size of the evaporated area. Those results give us an estimation of the laser beam shape on the sample.

3.6 Cleaning study

3.6.1 Cleaning effect

We vary the power and illumination time of a graphene sample to get an overview of the cleaning effect at different laser parameters. We measure a series of illumination times for each power setting. To hit the site of interest with the highest power density, we aim for the middle of a square in the TEM support grid.

A 4096 by 4096 pixels image of an area of 2048 by 2048 nm is taken of the hole before and after the illumination. According to Section 2.1, at this resolution the smallest detectable clean area is 1×1 nm^2. The difference in clean pixels we call the cleaning effect.

3.6.2 Center clean

In the center of the Gaussian laser beam, the photon flux is at its maximum. So the maximum cleaning should occur here. Therefore, we define the cleaning effect in the center as the cleaning effect of the system.

We first quantify the cleanness of three holes close to the laser target before illumination to ensure we hit the center hole. Then, the hole in the center of the laser spot provides an acceptable estimate of the cleaning effect.

3.6.3 Cleaning map

The maximum expected scanning range in STEM mode is 2×2 µm^2. Because the laser spot is much bigger than this, we also need to study the aloof effects of cleaning.

We therefore take a cleaning map as shown in Figure 3.8. For this map, we measure the cleaning effect like in 3.6.1 at every marked hole. We define the cleaning effect of a destroyed hole as 0, because the algorithm subtracts vacuum from the hole area which will be 0. This therefore avoids a division by 0 and directly shows that no cleaning is detected which is true for a non existing surface. The holes of interest are arranged in a star-like pattern to capture most of

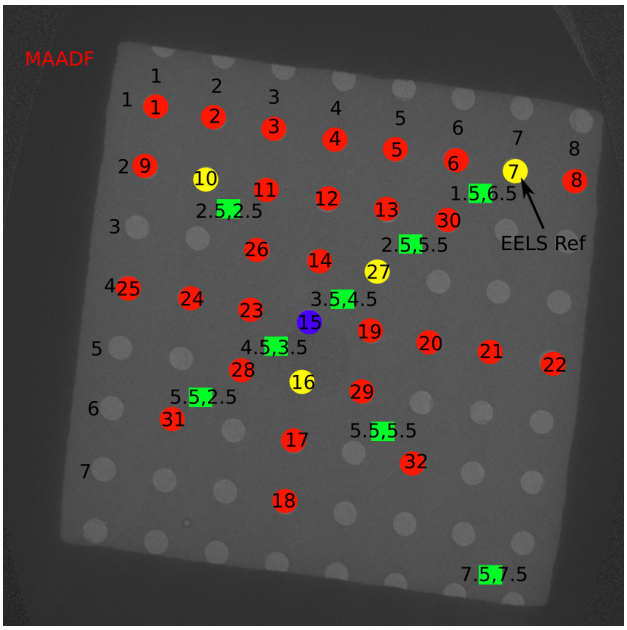

Figure 3.8: The map is taken at holes in a star pattern from the middle of the laser spot to quantify the aloof effects of the laser. For each map, 25 holes are scanned at 4096 by 4096 pixels in an area of 2048 by 2048 nm.

the aloof effects. We chose the cleaning parameters to match previous experiments and real-life use.

3.7 sEELS/sEEGS feasibility study

To detect the possibility of stimulated electron energy gain spectroscopy (sEEGS)/stimulated electron energy loss spectroscopy (sEELS), we use a thermally stable sample as described in Section 3.4.4. This CNT network/graphene sample contains an area with nanostructures. In the vicinity of this nanostructure, the probability of a laser-induced field interacting with electrons is much higher.

We select $0.1\,\mathrm{eV}$ for the EELS dispersion and move the ZLP so only the gain side is visible. Before the experiment, irradiating onto a sacrificial sample verifies the laser alignment. The laser power is set to the highest stable power of the laser ($80\,\mathrm{mW}$). Before and during laser illumination, we measure electron energy gain spectra. We capture the integral of the whole area in scanning mode for the EEGS signal. Therefore, drift does not affect the signal due to a fixed beam position. The difference between the two EEGS signals determines if we detect any effect. This gain effect should occur at $2.6\,\mathrm{eV}$ for a laser with a wavelength of $473\,\mathrm{nm}$.

3.8 Data analysis

3.8.1 Characterization of the optical microscope

On each point of interest along the optical axis (x-axis), the sub-images obtained by the experiment merge to a spot image. Each sub-image has its x, y, and z coordinates saved in its file name in mm. These coordinates tell us how to merge those sub-images. Where sub-images overlap, we use the mean value of each overlapping pixel.

Each image contains a light spot to which we manually fit a circle with diameter d using Nion Swift. The radius $r = \frac{d}{2}$ of each spot in internal stage coordinates is fitted along the optical axis. We repeat this also for the spot sizes measured without a lens, which we call parallel illumination. To determine the focal length of each lens, the slope (S_{lens}) and intersect I_{lens} is used to calculate the focus in internal stage coordinates:

$$f_{\text{relative}} = -\frac{I_{\text{lens}}}{S_{\text{lens}}} \ . \tag{3.1}$$

Further, the fit of a parallel measurement determines the position of each lens:

$$l_0 = \frac{I_{\text{parallel}} - I_{\text{lens}}}{S_{\text{lens}} - S_{\text{parallel}}} \ . \tag{3.2}$$

Finally the difference between the lens position (l_0) and the internal focus (f_{relative}) gives us the focal length (f_0):

$$f_0 = f_{\text{relative}} - l_0 \ . \tag{3.3}$$

3.8.2 Cleaning effect data analysis

To quantify the cleaning effect of a single-layer graphene Quantifoil sample, we fit a series of double-sided Gaussian peaks to the histogram of the scanned image. This fit gives us a vacuum peak if the graphene layer is ruptured or damaged and therefore representing a vacuum. We also can detect the peak of clean graphene and calculate its area using the double-sided Gaussian fit. Comparing the clean graphene area to the vacuum subtracted hole area gives us the ratio of the cleaned area. A comparison before and after cleaning delivers a quantization of the cleaning effect. Figure 3.9 is a flowchart of the complete analysis.

A series of n double-sided Gaussian curves shown in Equation 3.4 is fitted to a histogram of intensities obtained from MAADF scans:

$$\begin{aligned} f(x) = \sum_{0}^{n} \Bigg[& h_n \exp\Big(-4\log(2)(x - C_n)^2\Big) \\ & \cdot \left(\mathcal{H}(C_n) \exp\left(\frac{1}{\text{FWHM}_{n,r}^2}\right) - (\mathcal{H}(C_n) - 1) \exp\left(\frac{1}{\text{FWHM}_{n,l}^2}\right)\right)\Bigg] \ , \end{aligned} \tag{3.4}$$

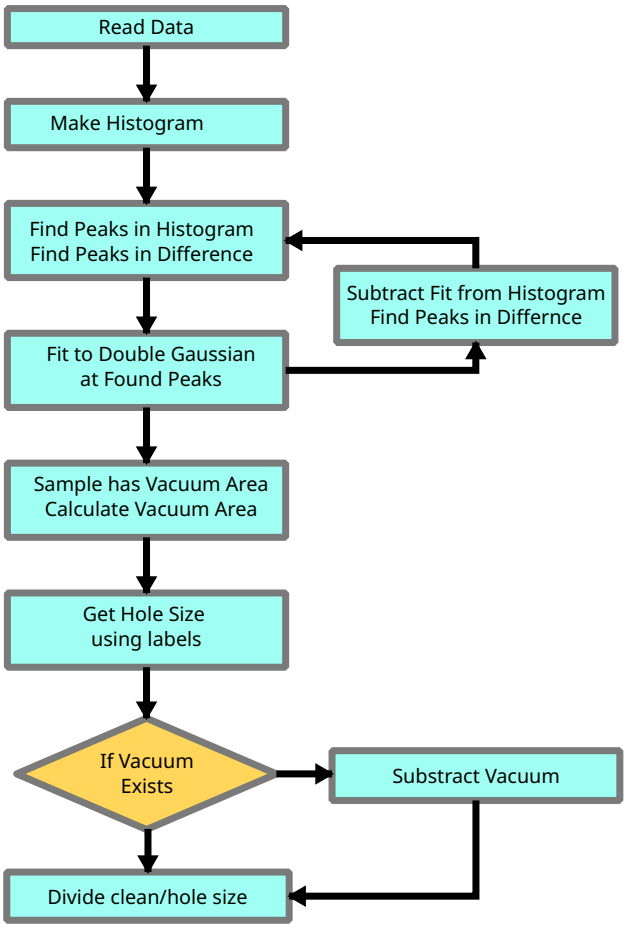

Figure 3.9: Flow diagram of clean analysis. First, we read the image data and create its histogram. We use a peak-finder to find the initial peaks in the histogram and fit Equation 3.4 to it. To obtain not yet detected peaks, we rerun the peak-finder on the difference between the histogram and the last fit. The algorithm now finds the fit for any sharp peak representing vacuum. Next, we analyze the size of the hole in the Quantifoil using "nd.label" from Scipy. Lastly, we calculate the relative clean area of the graphene in the hole.

where $\mathcal{H}$ is the Heavyside step function representing each side of the double-sided Gaussian, C_n is the center, and h_h the height of the detected peak. $\mathrm{FWHM}_{n,r}$ and $\mathrm{FWHM}_{n,l}$ are the full-width half-maximum values of each side of the Gaussian peak.

We use Equation 3.4 to fit the histogram using peaks found by find_peaks from the "SciPy.signal" library. We subtract the results from the previous fit from the original histogram for detection improvement at overlapping peaks. The peak_finder function is used again to find the peaks in this difference and adds them to the already detected peaks. The algorithm terminates when it does not find more peaks.

We test the first occurring peaks for vacuum criteria. First, all pixels that are within the first peak times 1.2 are labeled using "ndimage.label". If the variance of the labeled area $\sigma^2 < 10^{-8}$, the area is considered vacuum as we always managed to reliable detect the correct areas verified

by manual checking reference images. Therefore we subtract this vacuum area from the total hole area.

We use the position of the previously fitted histogram to calculate the area size of the hole. This data corresponds to the Quantifoil in the image corners.“ndimage.label“ then labels those regions. If their variance is $0.9 * 10^{-4} > \sigma^2 > 1 * 10^{-6}$, they are considered Quantifoil and therefore excluded from the clean-area calculation. We obtained this parameter by manually measuring the variance of known Quantifoil areas and adding an error margin.

The clean area of a site of interest is the area of the double-Gaussian fit corresponding to the clean peak. The first occurring peak after any vacuum peak is the clean peak. Additionally, it must have a lower index than 50 in the corresponding histogram, to avoid false positives. This parameter was obtained bay manually analyzing selected images with visible cleaning effect. If no clean peak is detected, we define the clean area as 0.

Further, we define the cleaning effect as the difference between the relative cleanness before and after a laser illumination of the same site of interest.

4 Results and Discussion

In this chapter, we characterize the optical properties of the optical microscope and laser. We measure and analyze the laser spot size of the sample. We further describe the developed *in-situ* laser system, its mechanical mounting, the optical components, the electronic controller, and the controlling software.

We now test and analyze the laser system for its cleaning capabilities and possible aloof effects. Finally, we evaluate the feasibility for sEEGS experiments.

4.1 Design of the laser system

4.1.1 Optics characteristics

Because of the poor documentation of the internal components of the optical microscope K2DistaMax, we need to check if they are suitable for laser use. To achieve this, we analyze each lens inside the microscope. The analysis follows the method discussed in Section 3.1.2.

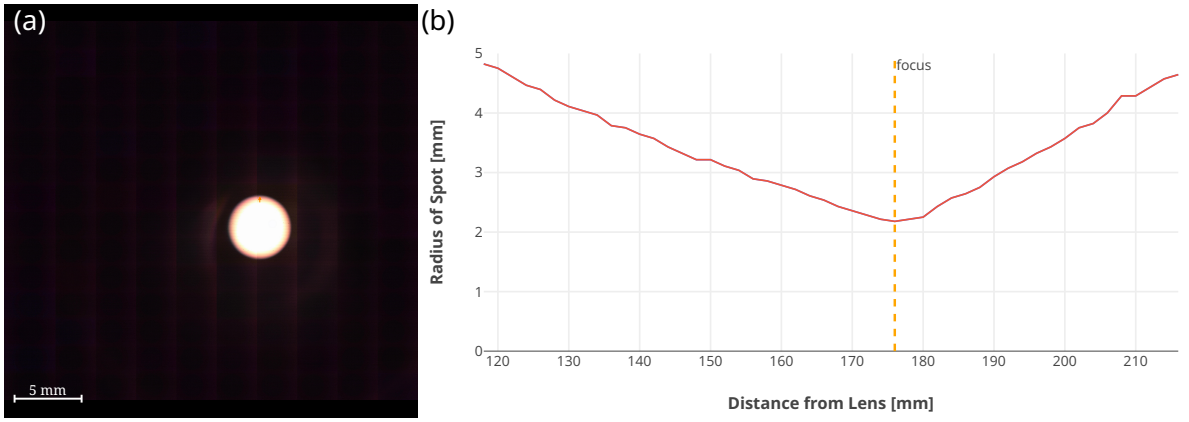

Figure 4.1: (a) Example image of a spot using a merged image at one z position.(b) Plot of the spot depending on the distance from the lens. The focal length is detectable.

The images taken of the light spots are now merged into a single image for each z-position using the analysis from Section 3.8.1. The radius of these spots is now manually measured using Nionswift. Figure 4.1 shows an example, where (a) is an image of the spot in focal position and (b) is a measured ray-tracing diagram. With this analysis and the help of a dataset of the pure probe, we can determine the focal length of the lenses, as shown in the figure. The divergence of the probe from being purely parallel is $3.75 \cdot 10^{-3}$ and therefore negligible.

Table 4.1: We order the focal length of each lens inside the optical microscope by its distance to the objective lens. f_0 is the focal length in the direction of the objective lens and f_1 in the opposite direction, as not all lenses are symmetric. Some lenses do have multiple focal points. For the lens at $438.54\,\mu m$, we did not measure data in the objective direction due to the geometric limitations of the setup.

Distance [mm]	f_0[mm]	f_1[mm]	Comments
0	294.0	323.0	Objective lens, origin of distance
63.28	482.0	514.0	—
97.4	180.0	234.0	—
99.6	-58.0	173.0	—
(108.1, 136.8)	-201.0	-211.0	Lens distance is variable (min, max)
(147.7, 119)	-103.0	-108.0	Lens distance is variable (min, max)
177.9	194.0	189.0	—
178.7	-159.0	-210.0	—
348.27	-99.0	-101.0	—
(369.8, 413.9)	-62.0	-38.0	Lens distance is variable (min, max)
(436.7, 454.2)	-62.0	-13.0	Lens distance is variable (min, max)
438.54	—	-2758.0	f_0 was not measured

Each lens has two focal points on either side of the lens. If the focal lengths of both lenses from Table 4.1 are within their uncertainties, the lens is considered symmetric. The microscope consists of different lens types, like achromatic lenses. Four lenses are mounted at variable positions to enable dynamic focusing and alignment. Due to geometric limitations in the setup, the lens at $438.54\,\mu m$ distance is only measured in one direction.

This approach is overly complicated because it is slow and needs extensive analysis. A better way is to use dedicated devices for lens measurements.

4.1.2 Optical path

We design the optical path of the laser beam as shown in Figure 4.2. First, it passes a digital single-lens reflex (DSLR) shutter before being shaped by additional lenses. A $180°$ free-space coupler leads the beam into the optical microscope. We use this to align the beam. Finally, the microscope focuses the laser beam onto the target inside the STEM. The beam alignment uses iris-diaphragms.

The whole optical system has an estimated power loss of $60\,\%$ measured at a laser output power of $25\,mW$. We measure the power at the laser output, before the mirrors, before the optical microscope, and after passing the optical microscope. To estimate the power loss, we measure the laser power at the objective lens with a black-body laser power meter.

We expect the optical microscope's power loss to transfer into its lenses. However, the light did not damage the lenses or the microscope. Laser power as a parameter is not an accurate

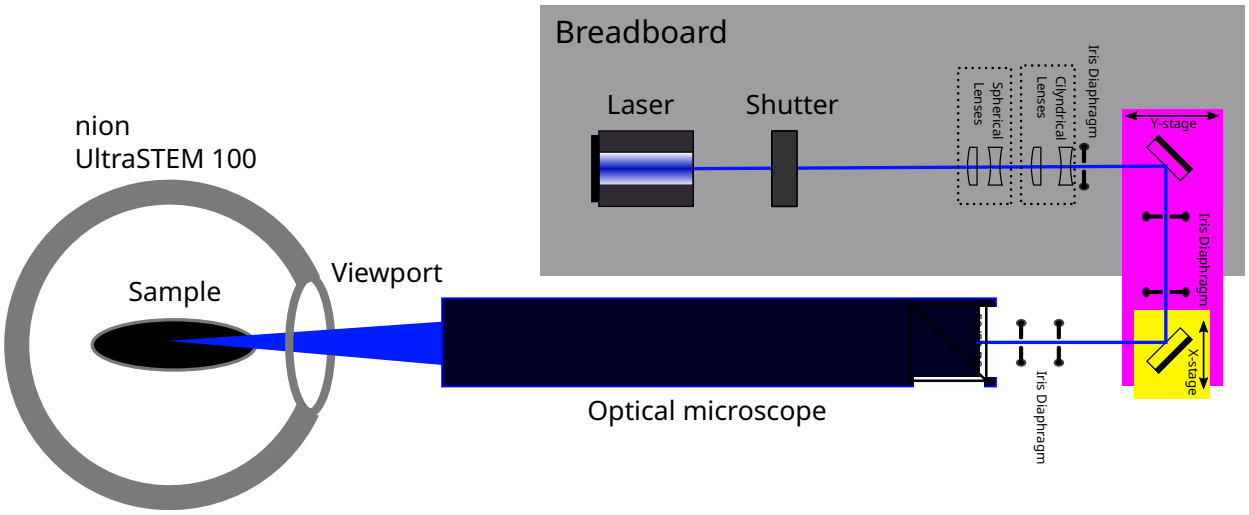

Figure 4.2: The optical path of the laser beam: the parallel laser beam first passes the mechanical shutter and then some additional lenses for coupling the laser to the optical microscope. Afterwards, 2 $45°$ mirrors align the beam to couple it into the optical microscope. The microscope focuses the beam onto the sample inside the electron microscope.

estimate for sample temperature. The heat transfer varies based on sample holders and materials of interest.

4.1.3 Quantifoil absorbency

To help choose a laser wavelength, we performed a quick light absorbency test with an empty Quantifoil support grid. Therefore, we use an optical transmission microscope with a scientific CCD camera. Because the camera splits its red-green-blue (RGB) channels, we can make a rough estimate for the wavelength with the best absorbency.

Figure 4.3 plots the transmission for three channels along the orange line. You can see the fully transmitted light in the absence of the support grid and at holes in the Quantifoil support grid. In between those holes, the transmission through the Quantifoil is visible. The blue channel shows slightly more absorbance than the red and green channels. Because of these results, we chose a blue laser for our setup.

4.1.4 Laser spot on the sample

To estimate the laser spot size on the sample, we use the laser system to evaporate a pure Quantifoil sample at different illumination times. Afterward, an elliptical contrast difference at the Quantifoil is visible. This ellipsis originates from the Quantifoil thinned by the laser pulse.

We fit an ellipsis to the thinned Quantifoil visible in CCD mode as shown in Figure 4.4. The hole sizes of the grid define the length scale calibration. Three different laser Powers ($10\,$mW, $15\,$mW and $20\,$mW) where chosen to obtain those ellipses.

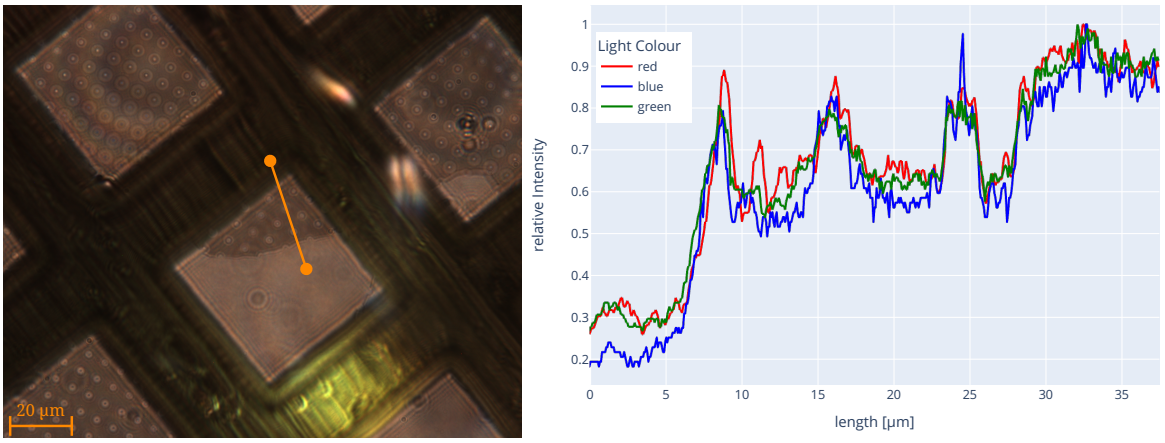

Figure 4.3: (a) Optical transparency along the line on a Quantifoil grid. We split the transparency into RGB channels. The Quantifoil absorbs slightly more light in the blue channel than in the other channels.

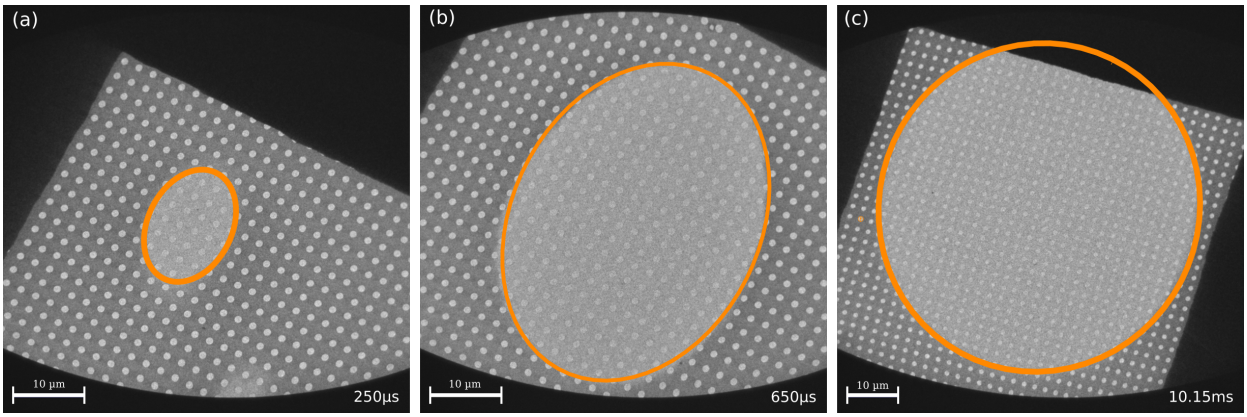

Figure 4.4: Visible Quantifoil thinning due to laser irradiation: The Images show the sample after pulses with $15\,\mathrm{mW}$ at different pulse lengths. You can see how increasing illumination times also increases the elliptical area from (a) to (c).

From these ellipses, we can use the pulse length (t_{pulse}) and the laser power (P_{laser}) to get an estimate of the power density ρ_P as shown in Equation 4.1:

$$\rho_P = \frac{1}{P_{\mathrm{laser}} * t_{\mathrm{pulse}}} \,. \tag{4.1}$$

We interpret the 0 on the x-axis as the ellipse center. For each ellipse, we put the estimated power density ρ_P to the corresponding length of the ellipsis axis. For each ellipsis, we see two data points mirrored about the x-axis.

From fitting a Gaussian curve to the power density, we estimate the FWHM of the Gaussian laser beam profile at the sample shown in Figure 4.5. For the width of the ellipsis we get $\mathrm{FWHM}_w = (29 \pm 1)$ µm and for its height $\mathrm{FWHM}_h = (35 \pm 1)$ µm. These values are close to our expectations at the start of the project.

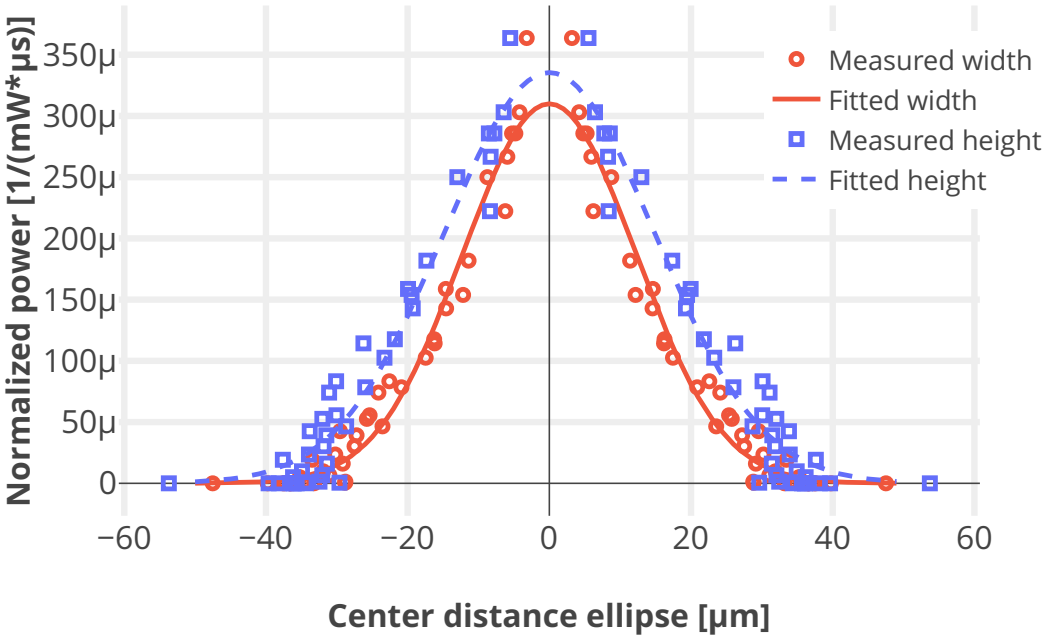

Figure 4.5: We fit an ellipse to the visible contrast of the Quantifoil thinning and measure both axes. The reciprocal illumination time divided by the laser power represents a normalized power density shown in the graph. A Gaussian function is fitted to these density values to obtain the FWHM of the laser profile as it is at the sample.

4.1.5 Mechanical design

The mechanical design of the *in-situ* laser system prioritizes stability and modularity. This system, together with its optics, alignment screws, and controls, is developed as a detachable module at the microscope. Due to microscope maintenance, the module must be able to be dismounted and mounted back in again.

This thesis needs to achieve stability and precise alignment. Therefore, we design a custom 2-way gimbal with double ball bearings to mount the optical microscope. This gimbal enables precise angular control for alignment and more stability than with off-the-shelf components for cameras. For alignment in $200\,\mathrm{mm}$ distance from the gimbal, two micrometer screws in a custom spring-mounted stage align the angle. The laser beam is coupled to the optical microscope using perpendicular linear micrometer-stages. the Coupling happens in an Angle of $180°$ so the optical microscope is hit precisely. the vertical angle of the optical microscope is aligned using a rotary stage rotating around the y-axis. Because of the coupler height and the laser thermal output, we design an Al-holder with an optional heat sink.

All those components were designed using "SolidWorks 2019" and produced in cooperation with our in-house mechanical workshop using a computerized numerical control (CNC) mill.

This setup uses an optical table with a 25 by 25 mm M6 tap pattern as its base. The

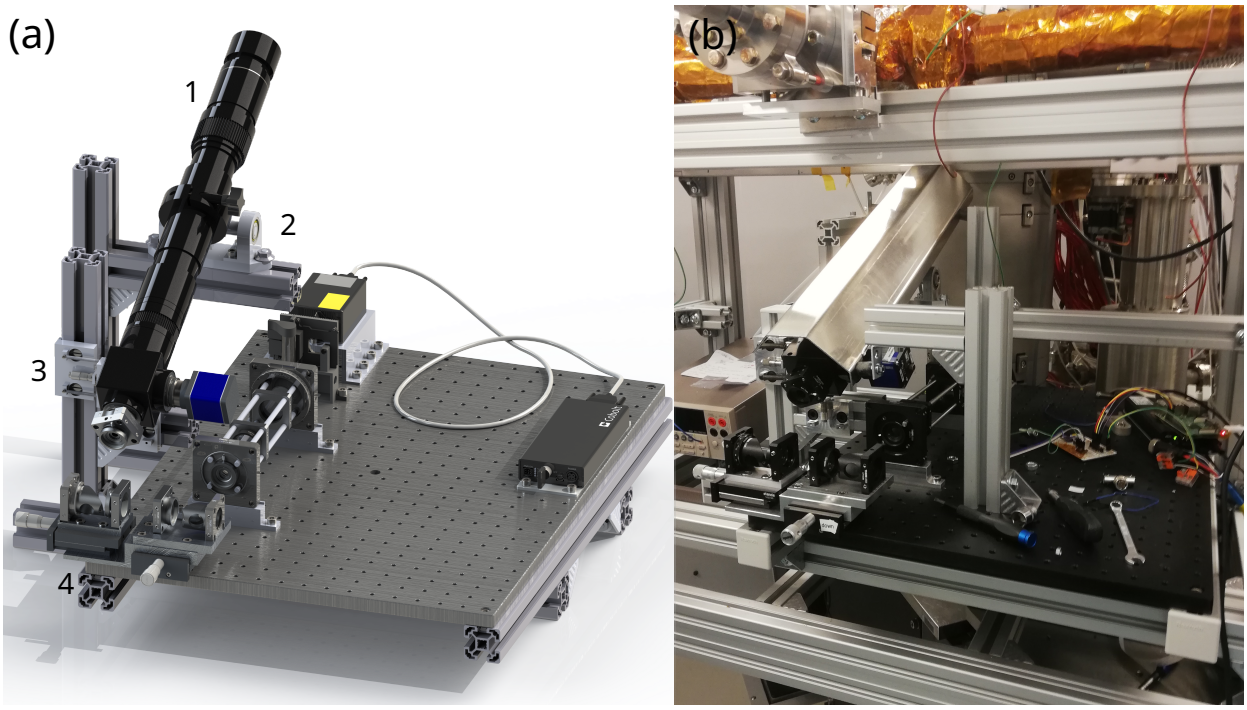

Figure 4.6: CAD drawing of the laser system: The optical microscope (1) mounts on a gimbal (2), and a custom angular stage (3) aligns it. A 2-axis linear stage (4) couples the laser beam into the optical microscope.

optical microscope with its alignment hardware is mounted using 40 mm by 40 mm Bosch-Rexroth aluminum profiles with a 10 mm groove. This removable module mounts onto the previously existing Bosch-Rexroth Al-profiles on the STEM air-table.

The vibration-sensitive optical microscope needs protection from user interference. We mount a protective aluminum cover with rubber buffers for additional damping protecting the microscope.

4.1.6 Mechanical shutter

It is crucial to control illumination times with an accuracy of 1 µs to achieve all the previously proposed *in-situ* applications. Therefore, users need to be able to control the shutter. Commercially available shutters for laser applications are either mechanical and slow (< 1 ms) or use optical properties of lasers, like accustic-optical modulator (AOM) or electric-optical modulator (EOM). Both solutions can achieve high precision in timing ($\sim$1 ns) but come with considerable downsides and high prices. EOMs need high voltages and precise alignment close to the electron microscope. AOMs can induce vibration close to the microscope. The design of the laser system must prevent those downsides.

In Photography, there is also a need for shutters with similar properties. single-lens reflex (SLR) cameras solved this problem by implementing two curtain shutters into one, the first in the open and the second in the closed position. This OEM design can achieve a shutter fulfilling our requirements.

These shutters are OEM for cameras and need additional electronics to work as stand-alone. Therefore, we need to develop those electronics.

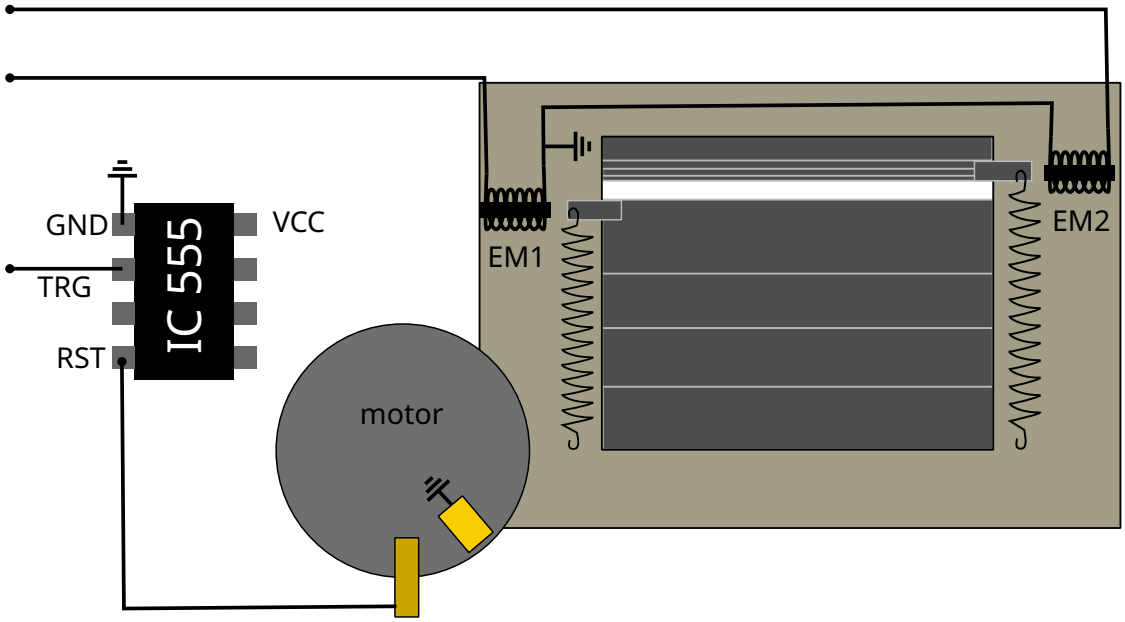

Figure 4.7: Schematic representation of the shutter: EM1 and EM2 are activated, keeping the spring-loaded curtains in place. If you turn off EM1, the shutter opens, and EM2 closes the second curtain. After the shutter pulses, it needs to retension. An IC-555 timing chip starts the motor and resets if the motor is in the shutter-ready position.

We use a DSLR Shutter assembly from a Cannon 60D for illumination time control. These are double curtain shutters with two independently operating curtains Figure 4.7. The curtains are spring-loaded and held in place by electromagnets. In a ready state, one curtain is in the open position while the other curtain is in a closed position. To open the shutter, we remove the power supply to the electromagnet holding the curtain in a closed position. To close it, we remove the other electromagnet's power. The delay between the curtain activations is managed by a Raspberry Pi using its general purpose input output (GPIO) pins. After the open/close circle, the springs need to be re-tensioned. Therefore, we turn the electromagnets on again, which triggers an IC-555 [76] flip-flop. A motor turns until the springs are under tension, initiated by the same IC-555. A sliding contact at the motor illustrated in Figure 4.7 resets the IC-555 when the shutter is tensioned. The complete cycle of tension and ignition is listed here:

1. Activate shutter electromagnets
2. Strart Motor to open reset contact
3. Start IC-555 for re-tension until reset
4. Turn the first electromagnet off to open the shutter
5. Turn the second electromagnet off to close the shutter after a predefined delay

To connect the shutter to the Raspberry Pi, NPN transistors convert the shutter voltage $12\,\mathrm{V}$ voltage at the common collector (Vcc) into the $3.3\,\mathrm{V}$ logic voltage of the Raspberry Pi.

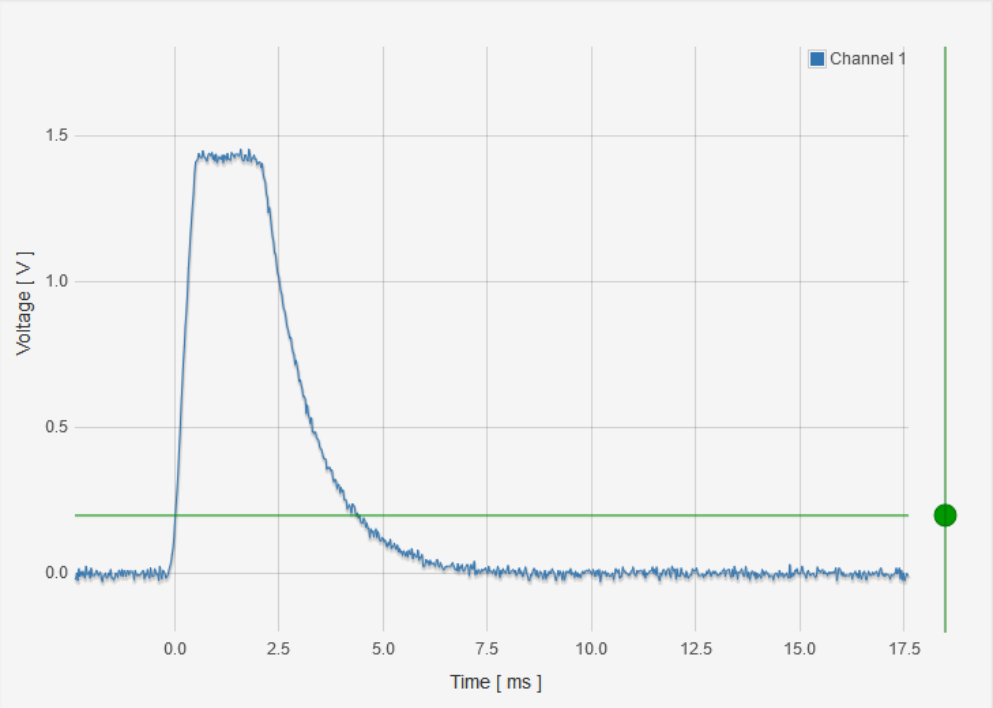

Figure 4.8: Measured shutter speed using a photoelectric barrier coupled to an oscilloscope. The expected pulse length of the laser is $2\,\mathrm{ms}$. The slope at the onset and offset of the measured pulse is from the response times and the high resistances of the photodiode.

A photoelectric barrier measures the laser illumination times. We place a LED on one end of the shutter opposite a photodiode on the other end. When the shutter is open, the photodiode can detect the LED light. A RedPitaya measures the voltage with its oscilloscope mode shown in Figure 4.8. The shutter speed closely matches the expected pulse length. The tail is from the high resistance of the RedPitaya's measurement port.

4.1.7 System control and API

A Raspberry Pi controls the hardware of the laser system. To achieve this, it connects to a nionswift plugin via RESTful API [77] and Rabbit messageing queue (MQ) [78].

The control software uses Python and C. The C part does the time-critical work, as its execution time is way faster. We use Python for integration within the IT infrastructure and the user interface.

To start and operate the laser module, the nionswift control unit sends a RESTful API request to the laser-control unit. The laser-control unit turns on and off the laser module and operates the shutter. Their state, including the interlock, is continuously monitored to publish every event to the nionswift controller via Rabbit MQ.

The laser control unit operates the shutter via an IC-555 timing chip by pulse-width modulation

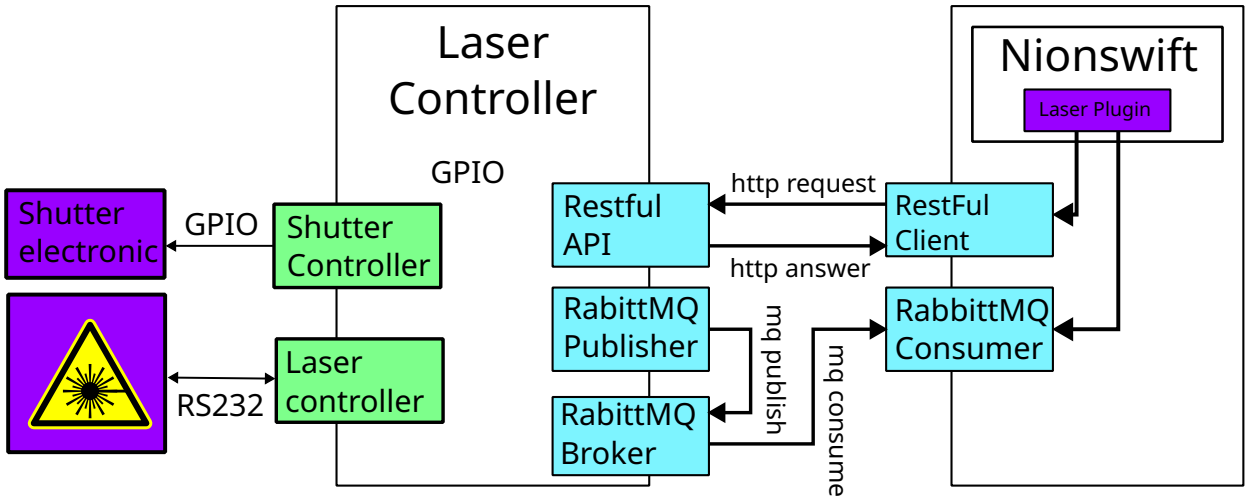

Figure 4.9: IT schematics of the laser control: The Laser Controller Raspberry Pi manages the mechanical shutter using a GPIO pin and communicates directly with the laser via an RS232 serial interface. A RESTful API interacts with input from the microscope's User PC running Nion Swift. Nion Swift is informed about the laser status via Rabbit MQ.

(PWM) from a GPIO pin. The laser controller is operated and monitored via its native RS232 interface.

4.1.8 Alignment of the system

The thermal heating effect helps us to align the system. Therefore, a Protochip heating chip covered with a DWCNT network connects to a Keithley multimeter. First, the middle of the chip is searched and brought to zero-defocus with the help of the DWCNT network. After turning the system on, the alignment screws help us to maximize the resistance of the heating chip.

One way to align the sample is continuous laser illumination and simultaneously measure the thermal EELS shift at the carbon edge at $284\,\mathrm{eV}$ and maximize the energy as measured in EELS. Therefore, we need a temperature-stable sample. A DWCNT network with graphene on top supported by a copper plate with a $400\,\mu\mathrm{m}$ hole promises to fulfill this requirement.

For a more precise alignment, we pulse a sacrificial sample. The difference between the aim and the hit enables further alignment using both coupling micrometer screws. By iterating this process, we can align the setup with $1\,\mu\mathrm{m}$ accuracy.

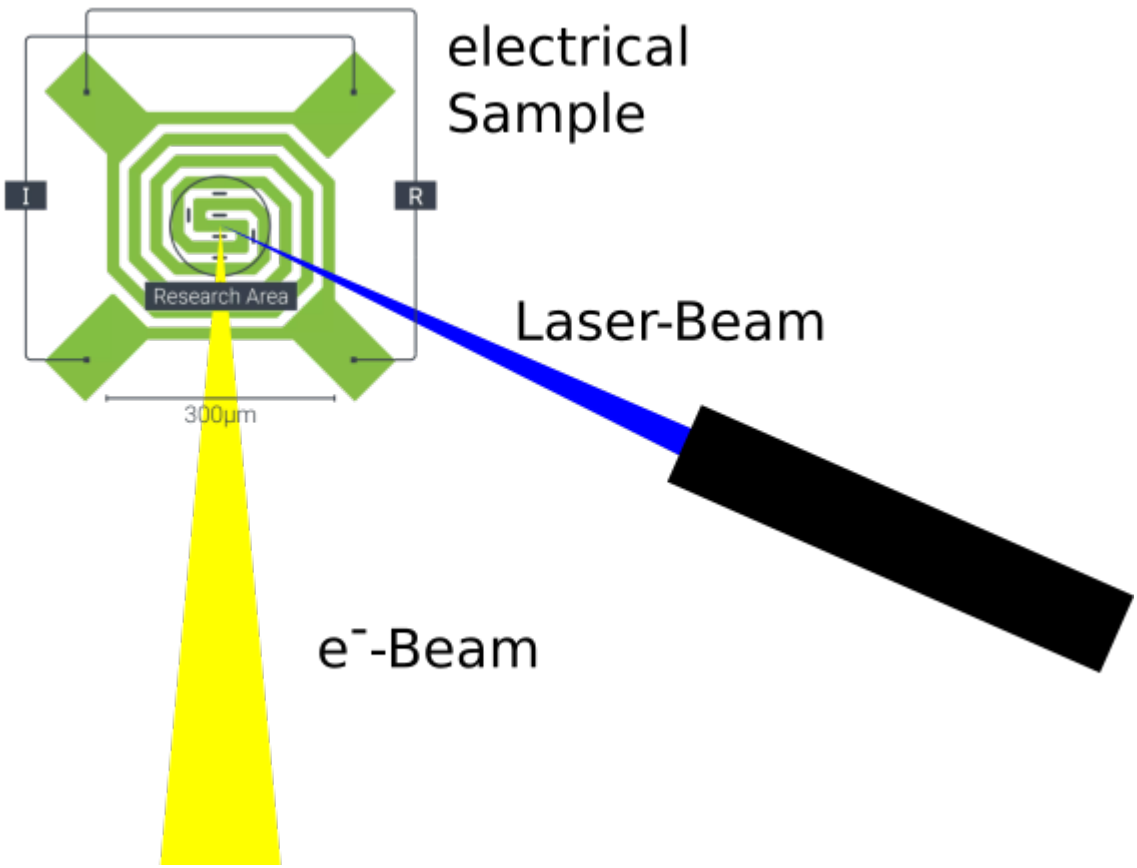

Figure 4.10: The laser and the electron beam shall coincide on the sample to align the laser. Therefore, we move the center of the sample under the electron beam at 0-defocus. Now, the laser is aligned to the middle of the sample using a 4-point measurement of the sample resistance.

4.2 *In-situ* cleaning of samples

4.2.1 Cleaning effect on graphene

As the primary design goal of the laser system is sample cleaning, we need to optimize the system parameters for cleaning graphene on Quantifoil grids. A sample cleaning study according to the procedure discussed in Section 3.6.1 helps us with it.

Figure 4.11 shows an example dataset of a cleaning experiment. (a) is a heat map of a contaminated sample, whereas (b) shows one after laser cleaning. (c) combines both intensity histograms of those heat maps. The first peak marked as "1" is the intensity of clean graphene as detected with MAADF. The region in the histogram marked with "2" is contaminated. "3" and "4" is the Quantifoil support grid. The analysis of those histograms leads to the conclusion that the Quantifoil grid has substantially thinned during laser illumination. Also, the dark blue areas marked as "1" have grown after the experiment. In the histogram, we can see a sharpened peak at this intensity. The smaller and sharper peak "2" indicates the removal of contamination

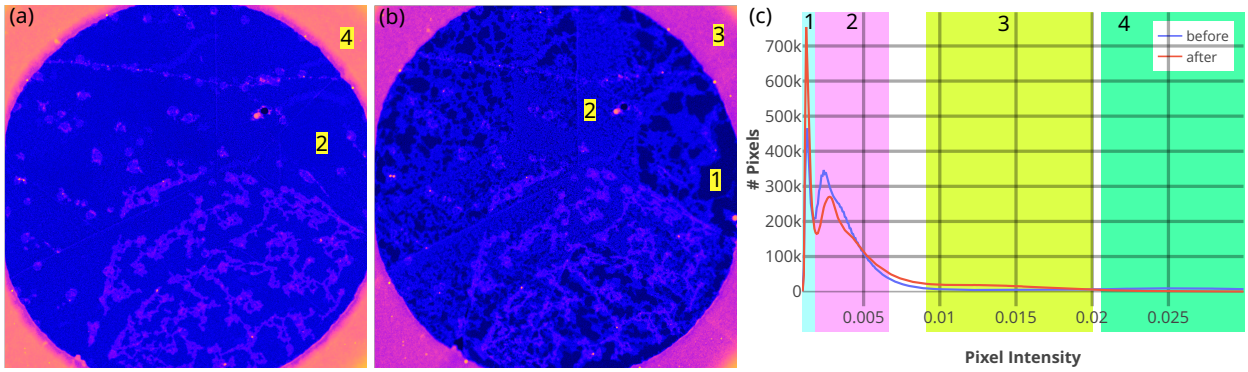

Figure 4.11: Dirty (a) and clean (b) MAADF image of a Graphenea graphene sample. (c) Histogram of the images with the respective peaks marked and linked to their corresponding features. (1) peak of clean graphene, which is significantly higher in the cleaned sample. (2) contamination peak. (3) and (4) Peaks assigned with the Quantifoil support film. A clear shift of those peaks is visible due to thinning from laser irradiation.

there. Therefore, we conclude that the laser cleaning process works and cleans a substantially large sample area.

However, this effect needs closer quantification and further studies to choose the best cleaning parameters and to examine its reproducibility.

Analyzing the cleaning effect of in-situ laser cleaning, we measure the sample cleanness before and after cleaning. For quantification, the clean peak in comparison to the hole size defines the relative cleanness according to 3.8.2. For this experimental series laser powers of $10\,\mathrm{mW}$ $15\,\mathrm{mW}$ and $20\,\mathrm{mW}$ are chosen. the cleaning effect is measured at $t = (100 \cdot 2^n)$ µs illumination time. Where n is an integer between 0 and 6.

Figure 4.12 shows the relative cleaning effect for each laser power concerning its illumination time. As soon as sample destruction develops, we don't plot any more data. For the 10mW laser power dataset, no destruction occurs even after long illumination times. We detect the most relative cleaning at a laser power of $20\,\mathrm{mW}$, but destruction starts soon after that. Because of this, we don't consider $20\,\mathrm{mW}$ as a safe laser illumination power for cleaning. Although the cleaning effect is sufficient in this setting, there is a high risk of destruction. Using $10\,\mathrm{mW}$ as laser power needs long illumination times to measure a cleaning effect. Nevertheless, there is no risk of destruction. Therefore, the best parameters for cleaning graphene on a Quantifoil grid are $1.6\,\mathrm{ms}$ at $15\,\mathrm{mW}$ laser-power.

4.2.2 Cleaning map on graphene

The same methods as discussed in Section 4.2.1 are used to map the cleaning effect over a greater area on the sample. Due to the large size of the laser spot concerning the site of interest, the maximum area size studied is one hole in the gold grid. We must know about the effects surrounding the site of interest if we operate delicate samples.

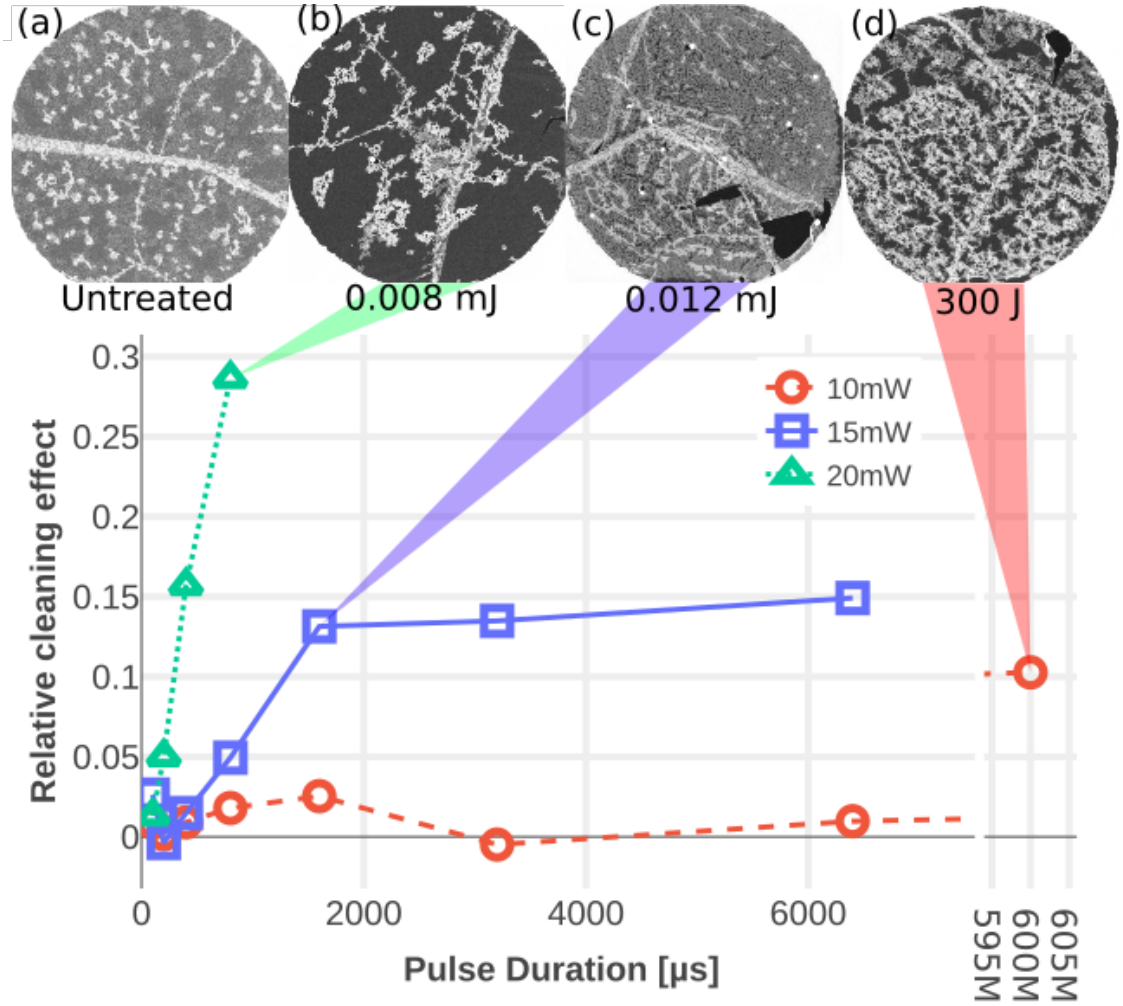

Figure 4.12: Cleaning effect with different laser power: The difference between clean areas before and after the laser pulse. The size of clean areas relative to the hole area is called the relative clean area. The relative cleaning effect is their difference. The curves in the plot stop at the point when sample destruction occurs, except for the 10 mW experiment, where we did not see destruction. (a) shows an untreated sample. (b) has the most cleaning effect at the highest power at 20 mW. (d) and (d) have lower cleaning effects but also less destruction of the sample, although the overall laser energy increases.

For this map, 25 holes are scanned at 4096 by 4096 pixels in an area of 2048 by 2048 nm in a star-shaped pattern. Where the middle of the star coincides with the laser spot. As cleaning parameters we chose 1 ms illumination time at a laser power setting of 20 mW. These settings give us a high chance for a relative cleaning effect of 0.25 according to Figure 4.12.

Figure 4.13 shows that the highest cleaning effect occurs close to the laser spot's center. On the rim and outside close to the rim, we see a negative cleaning effect. The maximum relative cleaning effect does not exceed 0.15. These results are not as high a cleaning effect as we expected beforehand but still high according to Section 4.2.1.

The contamination at the borders of the laser spot could be recontamination with evaporated material from the center. We also can see that the highest cleaning does happen in the middle but close to the middle of the laser spot. We attribute this to recontamination and the high thermal conductivity of graphene.

During laser illumination, we also can see extensive thermal sample drift. Such a drift happens due to the thermal vibrations of the sample. These vibrations are also suspected to influence clean regions and sample recontamination. However, at a distance of 2 times the laser spot size, we can't see recontamination or cleaning anymore. Therefore, on a graphene sample on a Quantifoil grid, one should only use the laser at least 75 µm away from any delicate area.

4.2.3 Evaporated material

We use a mass spectrometer, seated outside the column at the sample exchange, to estimate the chemical composition of the sample contamination. Because of this geometry, we could have failed to detect contamination while illuminating the sample. Another reason could be that the laser evaporates a small amount of material because the FWHM of the laser spot is at roughly 30 µm. Therefore, a mass spectrometer might struggle to detect the contamination.

This material also contaminates the sample at a different, not laser-illuminated, spot. In Figure 4.13, we observe this effect as a negative relative cleaning effect at holes close to the illuminated area. Therefore, we conclude that all contamination, removed by laser illumination, reattached itself to the sample after evaporation. Also, the contamination did not evaporate in the first place and migrated on the sample to spots less affected by heat.

4.2.4 Stability of cleaned samples

The in Section 4.1.4 discussed Quantifoil thinning by laser illumination affects sample stability. In particular, it makes the sample less stable towards vibrations, which increases the difficulties in obtaining atomic resolution. The cleaner a sample becomes, the more difficult it gets to obtain high resolution on those clean sample parts.

As we can see in Figure 4.11(b), the contamination seems to stick onto impurities such as grain boundaries.

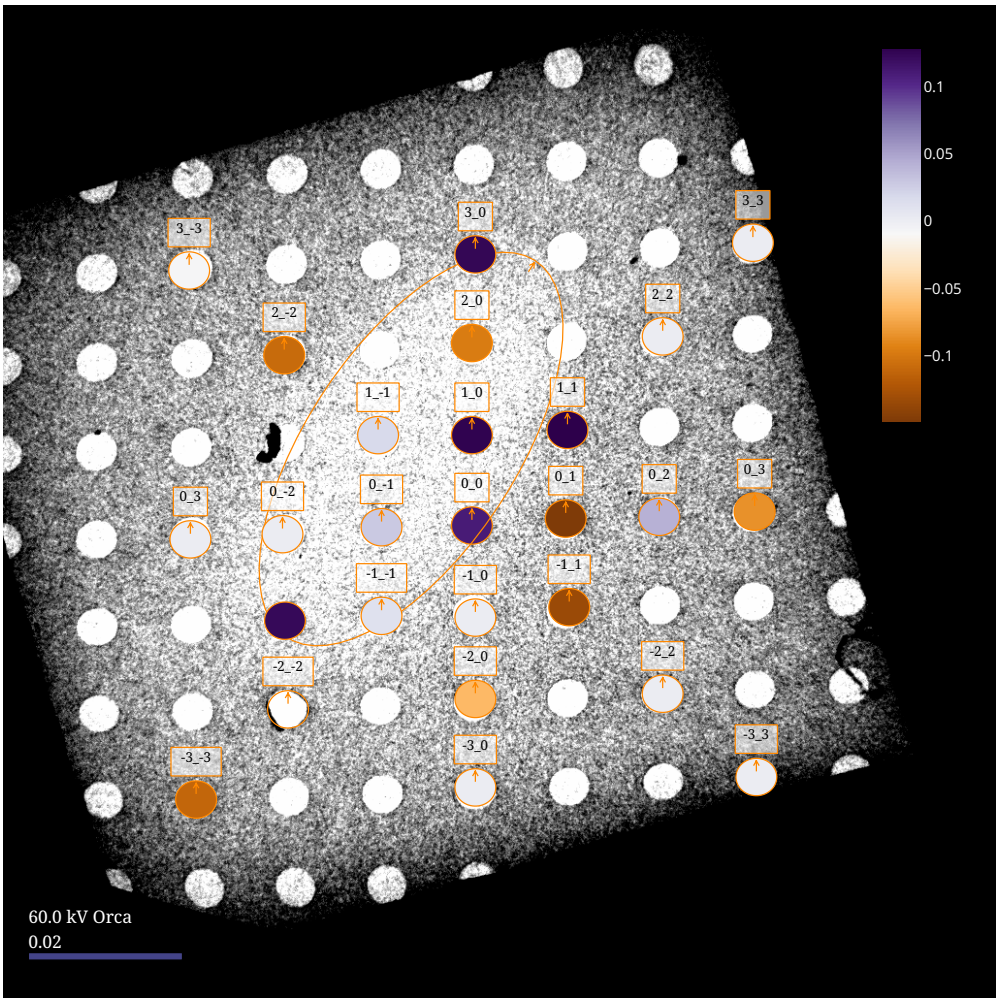

Figure 4.13: Cleaning effect map of a large area: the light spot in the middle is where the laser beam hit the sample. Close to the center, the cleaning results are the best. Also, some outer areas accumulate more dirt during the cleaning process.

These results let us suspect that contamination can stabilize the sample towards vibrations and, as a result, enable atomic resolutions.

4.2.5 Sample damage

By laser-cleaning the sample, we can damage it because of thermal effects and vibration. Sample material like thin graphene layers can break apart and get destroyed. Support material, like Quantifoil, can crack and break apart, destroying the sample. The end of the graphs from Figure 4.12 indicate sample destruction, showing the maximum parameters suitable for cleaning.

4.2.6 Other sample materials

The laser cleaning method described in Section 4.2.1 can also be used for other sample types, different in their support material and material of interest like exfoliated hexagonal boron nitride (hBN), graphene on SiN grids, and MoS_2

4.3 Proof of concept for sEELS/sEEGS

As discussed in Section 2.6, a laser attached to an electron microscope can enable second-order electro-photon interaction experiments. In this thesis, we perform said experiment and estimate its feasibility using our new laser system. The laser must operate at its highest power setting to give us a high enough possibility for detection. Also, long EELS/EEGS integration times and spatial statistics are needed as samples tend to drift during laser illumination. Due to the laser operating in its highest power setting, a high energy density on the sample can lead to problems such as destruction or thermal drift. Sample destruction needs a design for a temperature-stable sample (Section 3.4.4).

4.3.1 EELS/EEGS spectra

For this proof of concept study, the sample from Section 3.4.4 was illuminated with a laser in continuous mode at its highest possible energy of $80\,\mathrm{mW}$. As the sample consists of graphene and CNTs, a sufficient amount of nano-structures can contribute to photon-electron coupling.

Maximizing the possibility for photon-electron interactions, we average all EEGS spectra. We measure these spectra during laser illumination over a large sample area. As a single-spot measurement could probably hit anywhere on the sample, averaging reduces the effect of thermal drift. Spectra are measured without laser illumination at this site of interest as a reference.

The EEGS spectra with and without laser illumination do not differ. The expected peak should be at $2.6\,\mathrm{eV}$ energy gain for a laser with a wavelength of $473\,\mathrm{nm}$. There is no peak in the first harmonic energy level.

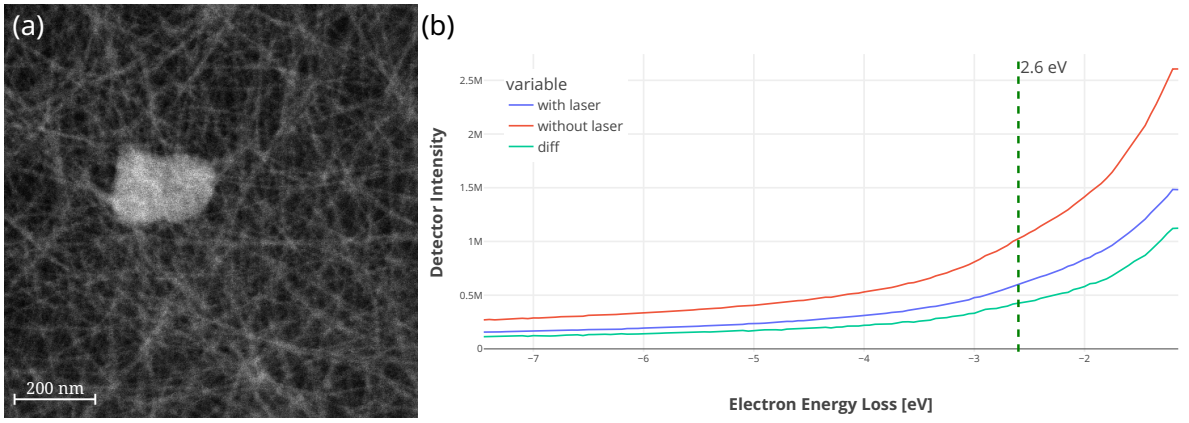

Figure 4.14: sEEGS: (a) in the presence of a nanostructure, we measure EELS with and without laser illumination. (b) EELS curves with and without laser illumination: the difference between those two is green. At $2.6\,\mathrm{eV}$ (photon energy of the laser), we don't detect a peak.

5 Conclusion

We successfully developed and deployed a *in-situ* laser system for our STEM. The optical microscope focuses the laser beam onto a spot with the width of (29 ± 1) µm and a height of (35 ± 1) µm. The system is controllable from outside the STEM room and fully integrated into Nion Swift for good usability.

The system showed successful cleaning on graphene with reasonably low cleaning parameters. We obtain the best cleaning results at $20\,\mathrm{mW}$ and $800\,\mu\mathrm{s}$ but suffer substantial damage using longer illumination times. The sweet spot for graphene cleaning is at $15\,\mathrm{mW}$ and $1600\,\mu\mathrm{s}$. With these parameters, we can clean up to $15\,\%$ and do not experience damage, even when exceeding an illumination time of $6\,\mathrm{ms}$.

After cleaning, we sometimes experienced recontamination while imaging with the electron beam. This recontamination stops after an additional short laser pulse.

We also tested a variety of other materials on different sample holders. The laser managed the cleaning of hBN on SiN sample holders and of exfoliated multi-layer graphene.

We measured electron energy gain spectra with and without laser illumination. As there is no peak at $2.6\,\mathrm{eV}$, we did not detect any electron-photon interaction with this laser system. Therefore, sEEGS seems not feasible within our current system. We could increase the laser power by decreasing the focal point or exchanging the laser. In both cases, the power can become too high for non-destructive measurements, as we are already in a destructive regime. Another challenge is the tail of the ZLP, which could mask the $2.6\,\mathrm{eV}$ peak.

We can also use laser illumination to heat samples. As the laser setup is outside the electron microscope's column, there is no need for special sample preparation or specialized sample holders.

On the upside of laser heating, we can perform electrical experiments while heating without sacrificing pins. This new setup lets us shoot the laser at specialized sample holders like tilt holders or pre-prepared samples from other facilities. Also, spontaneous heating experiments can be carried out without sample transfer or sourcing new samples on heating devices.

On the downside, there is no direct feedback on the sample's temperature, leading to imprecise temperature control. Also, different samples and support materials react differently to laser illumination, depending on their optical and thermal properties, so each sample needs a new calibration.

The laser system proves to be useful for cleaning and heating samples. We use its cleaning capabilities already to obtain clean areas while study samples in the STEM [79, 80]. The concept

of *in-situ* laser cleaning can be deployed in every microscope with a clear optical view of the sample. Other materials need to be studied further to obtain the optimized cleaning parameters. We also showed that sEEGS with a continuous wave laser is hard to achieve if possible at all. The energy density for a reasonable sEEGS probability is high enough to damage the sample before measuring.

Bibliography

1. Hotz, M. T. *et al.* Optimizing the Nion STEM for In-Situ Experiments. *Microscopy and Microanalysis* **24,** 1132–1133. ISSN: 1431-9276, 1435-8115 (Aug. 2018).
2. Howie, A. *Electrons and Photons: Exploiting the Connection* in *Inst. Phys. Conf. Ser* **161** (1999), 311–314.
3. Tripathi, M. *et al.* Cleaning Graphene: Comparing Heat Treatments in Air and in Vacuum. *physica status solidi (RRL) – Rapid Research Letters* **11,** 1700124. ISSN: 1862-6270 (2017).
4. Shannon, C. E. A Mathematical Theory of Communication. *The Bell System Technical Journal* **27,** 623–656. ISSN: 0005-8580 (Oct. 1948).
5. Petersen, D. P. & Middleton, D. Sampling and Reconstruction of Wave-Number-Limited Functions in *N*-Dimensional Euclidean Spaces. *Information and Control* **5,** 279–323. ISSN: 0019-9958 (Dec. 1962).
6. Wallace, P. R. The Band Theory of Graphite. *Physical Review* **71,** 622–634 (May 1947).
7. Mermin, N. D. Crystalline Order in Two Dimensions. *Physical Review* **176,** 250–254 (Dec. 1968).
8. Mermin, N. D. & Wagner, H. Absence of Ferromagnetism or Antiferromagnetism in One- or Two-Dimensional Isotropic Heisenberg Models. *Physical Review Letters* **17,** 1133–1136 (Nov. 1966).
9. Novoselov, K. S. *et al.* Electric Field Effect in Atomically Thin Carbon Films. *Science* **306,** 666–669 (Oct. 2004).
10. Meyer, J. C. *et al.* The Structure of Suspended Graphene Sheets. *Nature* **446,** 60–63. ISSN: 1476-4687 (Mar. 2007).
11. Geim, A. K. Graphene: Status and Prospects. *Science* **324,** 1530–1534 (June 2009).
12. Castro Neto, A. H., Guinea, F., Peres, N. M. R., Novoselov, K. S. & Geim, A. K. The Electronic Properties of Graphene. *Reviews of Modern Physics* **81,** 109–162 (Jan. 2009).
13. Balandin, A. A. *et al.* Superior Thermal Conductivity of Single-Layer Graphene. *Nano Letters* **8,** 902–907. ISSN: 1530-6984 (Mar. 2008).
14. Muñoz, R. & Gómez-Aleixandre, C. Review of CVD Synthesis of Graphene. *Chemical Vapor Deposition* **19,** 297–322. ISSN: 1521-3862 (2013).

15. Yi, M. & Shen, Z. A Review on Mechanical Exfoliation for the Scalable Production of Graphene. *Journal of Materials Chemistry A* **3,** 11700–11715. ISSN: 2050-7496 (May 2015).

16. Eletskii, A. V. Carbon Nanotubes. *Physics-Uspekhi* **40,** 899. ISSN: 1063-7869 (Sept. 1997).

17. Moore, K. E., Tune, D. D. & Flavel, B. S. Double-Walled Carbon Nanotube Processing. *Advanced Materials* **27,** 3105–3137. ISSN: 1521-4095 (2015).

18. Kumanek, B. & Janas, D. Thermal Conductivity of Carbon Nanotube Networks: A Review. *Journal of Materials Science* **54,** 7397–7427. ISSN: 1573-4803 (May 2019).

19. Pfeiffer, R. *et al.* Unusual High Degree of Unperturbed Environment in the Interior of Single-Wall Carbon Nanotubes. *Physical Review Letters* **90,** 225501 (June 2003).

20. Kempa, K. *et al.* Carbon Nanotubes as Optical Antennae. *Advanced Materials* **19,** 421–426. ISSN: 1521-4095 (2007).

21. Wang, Y. *et al.* Receiving and Transmitting Light-like Radio Waves: Antenna Effect in Arrays of Aligned Carbon Nanotubes. *Applied Physics Letters* **85,** 2607–2609. ISSN: 0003-6951 (Sept. 2004).

22. Sharma, A., Singh, V., Bougher, T. L. & Cola, B. A. A Carbon Nanotube Optical Rectenna. *Nature Nanotechnology* **10,** 1027–1032. ISSN: 1748-3395 (Dec. 2015).

23. Gommans, H. H. *et al.* Fibers of Aligned Single-Walled Carbon Nanotubes: Polarized Raman Spectroscopy. *Journal of Applied Physics* **88,** 2509–2514. ISSN: 0021-8979 (Sept. 2000).

24. Liu, K. *et al.* Van Der Waals-coupled Electronic States in Incommensurate Double-Walled Carbon Nanotubes. *Nature Physics* **10,** 737–742. ISSN: 1745-2481 (Oct. 2014).

25. Capano, M. A., McDevitt, N. T., Singh, R. K. & Qian, F. Characterization of Amorphous Carbon Thin Films. *Journal of Vacuum Science & Technology A* **14,** 431–435. ISSN: 0734-2101 (Mar. 1996).

26. Schwan, J., Ulrich, S., Batori, V., Ehrhardt, H. & Silva, S. R. P. Raman Spectroscopy on Amorphous Carbon Films. *Journal of Applied Physics* **80,** 440–447. ISSN: 0021-8979 (July 1996).

27. Hwang, J. Y., Kim, D., Jang, H., Lee, S.-Y. & Joo, Y.-C. Thermal and Electrical Properties Depending on the Bonding Structure of Amorphous Carbon Thin Films. *Electronic Materials Letters* **20,** 648–656. ISSN: 2093-6788 (Sept. 2024).

28. Krivanek, O. L. *et al.* Vibrational Spectroscopy in the Electron Microscope. *Nature* **514,** 209–212. ISSN: 1476-4687 (Oct. 2014).

29. Zobelli, A., Gloter, A., Ewels, C. P. & Colliex, C. Shaping Single Walled Nanotubes with an Electron Beam. *Physical Review B* **77,** 045410 (Jan. 2008).

30. Zobelli, A. Electron Knock-on Cross Section of Carbon and Boron Nitride Nanotubes. *Physical Review B* **75** (2007).

31. Common Sessions on Microscopy: New Techniques and Improvements in Microscopy (CST). *Biology of the Cell* **93,** 432–439. ISSN: 1768-322X (2001).

32. Krivanek, O. L. *et al.* An Electron Microscope for the Aberration-Corrected Era. *Ultramicroscopy* **108,** 179–195. ISSN: 0304-3991 (Feb. 2008).

33. Hage, F. S., Radtke, G., Kepaptsoglou, D. M., Lazzeri, M. & Ramasse, Q. M. Single-Atom Vibrational Spectroscopy in the Scanning Transmission Electron Microscope. *Science* **367,** 1124–1127. ISSN: 0036-8075, 1095-9203 (Mar. 2020).

34. De Abajo, F. J. G. & Kociak, M. Electron Energy-Gain Spectroscopy. *New Journal of Physics* **10,** 073035. ISSN: 1367-2630 (July 2008).

35. Nathan, M. I., Dumke, W. P., Burns, G., Dill Jr., F. H. & Lasher, G. STIMULATED EMISSION OF RADIATION FROM GaAs P-n JUNCTIONS. *Applied Physics Letters* **1,** 62–64. ISSN: 0003-6951 (Nov. 1962).

36. Davarcioglu, B. An Overview of Diode Pumped Solid State (DPSS) Lasers. **1,** 12 (2010).

37. Mansuripur, M., Connell, G. A. N. & Goodman, J. W. Laser-Induced Local Heating of Multilayers. *Applied Optics* **21,** 1106–1114. ISSN: 2155-3165 (Mar. 1982).

38. Asenjo-Garcia, A. & de Abajo, F. J. G. Plasmon Electron Energy-Gain Spectroscopy. *New Journal of Physics* **15,** 103021. ISSN: 1367-2630 (Oct. 2013).

39. Das, P. *et al.* Stimulated Electron Energy Loss and Gain in an Electron Microscope without a Pulsed Electron Gun. *Ultramicroscopy. 75th Birthday of Christian Colliex, 85th Birthday of Archie Howie, and 75th Birthday of Hannes Lichte / PICO 2019 - Fifth Conference on Frontiers of Aberration Corrected Electron Microscopy* **203,** 44–51. ISSN: 0304-3991 (Aug. 2019).

40. Barwick, B., Flannigan, D. J. & Zewail, A. H. Photon-Induced near-Field Electron Microscopy. *Nature* **462,** 902–906. ISSN: 1476-4687 (Dec. 2009).

41. Cunge, G. *et al.* Dry Efficient Cleaning of Poly-Methyl-Methacrylate Residues from Graphene with High-Density H2 and H2-N2 Plasmas. *Journal of Applied Physics* **118,** 123302. ISSN: 0021-8979 (Sept. 2015).

42. Chen, J.-H., Jang, C., Xiao, S., Ishigami, M. & Fuhrer, M. S. Intrinsic and Extrinsic Performance Limits of Graphene Devices on SiO_2. *Nature Nanotechnology* **3,** 206–209. ISSN: 1748-3395 (Apr. 2008).

43. Li, Z. *et al.* Effect of Airborne Contaminants on the Wettability of Supported Graphene and Graphite. *Nature Materials* **12,** 925–931. ISSN: 1476-4660 (Oct. 2013).

44. Pálinkás, A. *et al.* The Composition and Structure of the Ubiquitous Hydrocarbon Contamination on van Der Waals Materials. *Nature Communications* **13,** 6770. ISSN: 2041-1723 (Nov. 2022).

45. Kaiser, U. A. Strategies for High-Resolution Imaging of Radiation-Sensitive Materials in an Aberration-Corrected Transmission Electron Microscope. *Microscopy and Microanalysis* **21,** 355–356. ISSN: 1431-9276, 1435-8115 (Aug. 2015).

46. Wang, Y. *et al.* Electrochemical Delamination of CVD-Grown Graphene Film: Toward the Recyclable Use of Copper Catalyst. *ACS Nano* **5,** 9927–9933. ISSN: 1936-0851 (Dec. 2011).

47. Li, C. *et al.* A Simple Method to Clean Ligand Contamination on TEM Grids. *Ultramicroscopy* **221,** 113195. ISSN: 0304-3991 (Feb. 2021).

48. Butz, B., Dolle, C., Halbig, C. E., Spiecker, E. & Eigler, S. Highly Intact and Pure Oxo-Functionalized Graphene: Synthesis and Electron-Beam-Induced Reduction. *Angewandte Chemie International Edition* **55,** 15771–15774. ISSN: 1521-3773 (2016).

49. Schweizer, P. *et al.* Mechanical Cleaning of Graphene Using in Situ Electron Microscopy. *Nature Communications* **11,** 1743. ISSN: 2041-1723 (Apr. 2020).

50. Shi, Z. *et al.* Patterning Graphene with Zigzag Edges by Self-Aligned Anisotropic Etching. *Advanced Materials* **23,** 3061–3065. ISSN: 1521-4095 (2011).

51. Lim, Y.-D. *et al.* Si-Compatible Cleaning Process for Graphene Using Low-Density Inductively Coupled Plasma. *ACS Nano* **6,** 4410–4417. ISSN: 1936-0851 (May 2012).

52. Felten, A. *et al.* Insight into Hydrogenation of Graphene: Effect of Hydrogen Plasma Chemistry. *Applied Physics Letters* **105,** 183104. ISSN: 0003-6951 (Nov. 2014).

53. Cheng, Z. *et al.* Toward Intrinsic Graphene Surfaces: A Systematic Study on Thermal Annealing and Wet-Chemical Treatment of SiO2-Supported Graphene Devices. *Nano Letters* **11,** 767–771. ISSN: 1530-6984 (Feb. 2011).

54. Chen, J.-H. *et al.* Charged-Impurity Scattering in Graphene. *Nature Physics* **4,** 377–381. ISSN: 1745-2481 (May 2008).

55. Gorantla, S. *et al.* A Universal Transfer Route for Graphene. *Nanoscale* **6,** 889–896. ISSN: 2040-3372 (Dec. 2013).

56. Yulaev, A. *et al.* Toward Clean Suspended CVD Graphene. *RSC Advances* **6,** 83954–83962. ISSN: 2046-2069 (Sept. 2016).

57. Ma, T., Miyazaki, K., Ariga, H., Takakusagi, S. & Asakura, K. Investigation of the Cleanliness of Transferred Graphene: The First Step toward Its Application as a Window Material for Electron Microscopy and Spectroscopy. *Bulletin of the Chemical Society of Japan* **88,** 1029–1035. ISSN: 0009-2673 (May 2015).

58. Lindvall, N., Kalabukhov, A. & Yurgens, A. Cleaning Graphene Using Atomic Force Microscope. *Journal of Applied Physics* **111,** 064904. ISSN: 0021-8979 (Mar. 2012).

59. Goossens, A. M. *et al.* Mechanical Cleaning of Graphene. *Applied Physics Letters* **100,** 073110. ISSN: 0003-6951 (Feb. 2012).

60. Moser, J., Barreiro, A. & Bachtold, A. Current-Induced Cleaning of Graphene. *Applied Physics Letters* **91,** 163513. ISSN: 0003-6951 (Oct. 2007).

61. Lin, Y.-C. *et al.* Graphene Annealing: How Clean Can It Be? *Nano Letters* **12,** 414–419. ISSN: 1530-6984 (Jan. 2012).

62. Algara-Siller, G., Lehtinen, O., Turchanin, A. & Kaiser, U. Dry-Cleaning of Graphene. *Applied Physics Letters* **104,** 153115. ISSN: 0003-6951 (Apr. 2014).

63. Her, M., Beams, R. & Novotny, L. Graphene Transfer with Reduced Residue. *Physics Letters A* **377,** 1455–1458. ISSN: 0375-9601 (Sept. 2013).

64. Thomas, H. R. *et al.* Deoxygenation of Graphene Oxide: Reduction or Cleaning? *Chemistry of Materials* **25,** 3580–3588. ISSN: 0897-4756 (Sept. 2013).

65. Ishigami, M., Chen, J. H., Cullen, W. G., Fuhrer, M. S. & Williams, E. D. Atomic Structure of Graphene on SiO2. *Nano Letters* **7,** 1643–1648. ISSN: 1530-6984 (June 2007).

66. Islam, A. E. *et al.* Atomic Level Cleaning of Poly-Methyl-Methacrylate Residues from the Graphene Surface Using Radiolized Water at High Temperatures. *Applied Physics Letters* **111,** 103101. ISSN: 0003-6951 (Sept. 2017).

67. Ferrah, D. *et al.* CF4/H2 Plasma Cleaning of Graphene Regenerates Electronic Properties of the Pristine Material. *ACS Applied Nano Materials* **2,** 1356–1366 (Mar. 2019).

68. Ferrah, D. *et al.* XPS Investigations of Graphene Surface Cleaning Using H2- and Cl2-based Inductively Coupled Plasma. *Surface and Interface Analysis* **48,** 451–455. ISSN: 1096-9918 (2016).

69. Infinity. *K2 DistaMax OEM Handbook* Sept. 2021.

70. Thorlabs. *CPS532 SpecSheet* (June 2017).

71. Krivanek, O. L. *et al.* Atom-by-Atom Structural and Chemical Analysis by Annular Dark-Field Electron Microscopy. *Nature* **464,** 571–574. ISSN: 1476-4687 (Mar. 2010).

72. Mangler, C. *et al.* A Materials Scientist's CANVAS: A System for Controlled Alteration of Nanomaterials in Vacuum Down to the Atomic Scale. *Microscopy and Microanalysis* **28,** 2940–2942. ISSN: 1431-9276, 1435-8115 (Aug. 2022).

73. *4contact-Measurement-Spiral-01.Png (WEBP-Grafik, 2067 × 1918 Pixel) - Skaliert (50%)*

74. *Resistance-v-Temperature.Png (WEBP-Grafik, 483 × 341 Pixel)*

75. Huebner Photonics. *Manual Cobolt 04-01* Aug. 2019.

76. Goyal, H. Understanding of IC555 Timer and IC 555 Timer Tester. **3** (2015).

77. Fielding, R. T. *Architectural Styles and the Design of Network -Based Software Architectures* PhD thesis (University of California, Irvine, United States – California). ISBN: 9780599871182.

78. Hong, X. J., Sik Yang, H. & Kim, Y. H. *Performance Analysis of RESTful API and RabbitMQ for Microservice Web Application* in *2018 International Conference on Information and Communication Technology Convergence (ICTC)* (Oct. 2018), 257–259.

79. Zagler, G. *et al.* Beam-Driven Dynamics of Aluminium Dopants in Graphene. *2D Materials* **9,** 035009. ISSN: 2053-1583 (May 2022).

80. Postl, A. *et al.* Adventures in Atomic Resolution in Situ STEM. *Microscopy and Microanalysis* **28,** 2342–2343. ISSN: 1431-9276 (Aug. 2022).